Estimating evapotranspiration in mountainous water-limited regions from thermal infrared data: Comparison of two approaches based on energy balance and evaporative fraction

Badr-Eddine Sebbar, Yoann Malbéteau, Saïd Khabba, Marine Bouchet, Vincent Simonneaux, Abdelghani Chehbouni, Olivier Merlin

Remote Sensing of Environment 315 (2024) 114481

Contents lists available at ScienceDirect

Remote Sensing of Environment

journal homepage: www.elsevier.com/locate/rse

Estimating evapotranspiration in mountainous water-limited regions from thermal infrared data: Comparison of two approaches based on energy balance and evaporative fraction

Badr-eddine Sebbar [a,b,*], Yoann Malbéteau [c], Saïd Khabba [a,d], Marine Bouchet [b], Vincent Simonneaux [b], Abdelghani Chehbouni [a,b], Olivier Merlin [b]

[a] Center for Remote Sensing Applications, Mohammed VI Polytechnic University (UM6P), Ben Guerir 43150, Morocco
[b] Centre d'Etudes Spatiales de la Biosphère (CESBIO), Université de Toulouse, CNES, CNRS, IRD, UPS, 31400 Toulouse, France
[c] Planet Labs Inc, San Francisco, CA 94107, USA
[d] LMFE, Physics Department, Faculty of Sciences Semlalia, Cadi Ayyad University, Marrakech 40000, Morocco

ARTICLE INFO

Editor: Jing M. Chen

Keywords:
Evapotranspiration
Mountains
Thermal-infrared
Topographic effects
Meteorological variability
Semi-arid

ABSTRACT

The pronounced impact of topography on meteorological conditions has largely limited evapotranspiration (ET) remote sensing techniques to relatively flat terrains. This study addresses this limitation by adapting and assessing the performance of two common ET models based on thermal infrared data in rugged mountainous regions: a physically-based energy balance model (TSEB-PT), and a contextual model (LST-VI). The latter derives the evaporative fraction (EF), defined as ratio of the latent flux (LE) to available energy, from spatial relationships between land surface temperature (LST) and Vegetation Index (VI), by assuming uniform meteorological conditions. The LST-VI model hence requires the normalization of LST data for meteorological variability effects induced by topography prior to EF estimation, while TSEB-PT requires the spatialization of meteorological data at the thermal sensor's resolution. This study provides for the first time a quantitative assessment of methods for correcting topographical effects at thermal data resolution within a steep-sided valley, and compares them when applied to EB- and EF-based models. Both ET models are applied to 30 m resolution Landsat data across a 20 km by 44 km area in the High Atlas mountain of Morocco from 2020 to 2022. The models' results are evaluated at two eddy covariance sites with or without considering topographic effects: an agricultural foothill site, and an elevated rocky site, located at 900 and 3850 m.a.s.l., respectively. By taking into account topography, the RMSE (and % error) on simulated LE at the foothill site was reduced by 29 W/m^2 (29 %) and 10 W/m^2 (16 %) for TSEB_PT and LST-VI respectively. At the elevated site however, the RMSE (and % error) reduction was 50 W/m^2 (50 %) and 64 W/m^2 (59 %) for TSEB_PT and LST-VI respectively. Analysis of the spatial variability over the study area indicates that the EF distributions (corrected for topographical effects) between east-facing and west-facing slopes are similar for LST-VI (mean difference of 0.01) and significantly different for TSEB_PT (mean difference of 0.19). Normalizing LST for topographic effects at the thermal sensor resolution is hence an effective way of estimating ET in mountains despite the inherent uncertainties in the available meteorological data.

1. Introduction

Globally, mountains represent about 39 % of continental surfaces and play a fundamental role in water availability and distribution (Viviroli et al., 2007; Viviroli et al., 2020). Often described as 'water towers' (Viviroli et al., 2007; Immerzeel et al., 2010), they capture more precipitation than their surrounding lowlands, and act as key reservoirs of water resources in regions otherwise marked by water scarcity. A prime example of such regions is Morocco, a country with a semi-arid climate, facing complex water resource management and allocation challenges, and home to prominent mountain ranges like the High Atlas and the Rif (Schulz and de Jong, 2004; Marchane et al., 2015; Baba et al., 2019; Hanich et al., 2022; Ouassanouan et al., 2022). In these ranges, both solid and liquid precipitations collectively contribute to a substantial 47–53 % of the groundwater recharge (Rhoujjati et al., 2023). Given their importance for water resources, a better understanding of

* Corresponding author at: 18 avenue Edouard Belin BPI 2801, 31401, Toulouse, Cedex 9, France / Lot 660, Ben Guerir 43150, Maroc.
E-mail address: badreddine.sebbar@um6p.ma (B.-e. Sebbar).

https://doi.org/10.1016/j.rse.2024.114481
Received 25 October 2023; Received in revised form 17 July 2024; Accepted 17 October 2024
Available online 30 October 2024

the hydrological dynamics and contributions of these 'water towers' is needed.

Quantifying evapotranspiration (ET) is one way of understanding the hydrological dynamics of these water-rich environments. This flux, which accounts for water evaporation from the land surface and transpiration by vegetation, provides key information on water loss to the atmosphere. An effective strategy to capture the spatio-temporal variations in ET, is the combination of process-based models and satellite remote sensing (Fisher et al., 2008; Jung et al., 2010; Miralles et al., 2011; Mu et al., 2011; Ryu et al., 2011; Wei et al., 2017). A diverse range of models has been developed, broadly classified into three main categories: ET models based on the water balance, ET models based on land surface temperature (LST) data, and ET models based on conductance formulations (Kool et al., 2014; Zhang et al., 2016; Chen and Liu., 2020). Among these, LST-based ET models are particularly advantageous in capturing spatial and temporal variations of ET in water-limited conditions using the LST images derived from remotely sensed thermal infrared data (Chen and Liu, 2020).

LST data can be used to feed three main categories of thermal-based ET models (Chen and Liu., 2020). The first and second categories comprise one-source and two-source ET models, both rooted in the surface energy balance (EB). These models utilize the LST data to estimate the sensible heat (H) and, subsequently, to compute the latent heat flux (LE) or the energy associated with the ET process as a residual of the EB (Bartholic et al., 1972; Soer, 1980; Norman et al., 1995; Bastiaanssen et al., 1998a, 1998b; Su, 2002; Norman et al., 2003; Allen et al., 2007; Kustas and Anderson, 2009). The third category encompasses the models based on the evaporative fraction (EF) defined as the LE to available energy ratio. In these models, EF is derived from an interpretation of the feature space defined by plotting LST as a function of a vegetation index (VI). EF is then transformed into ET given the available energy (Nemani and Running, 1989; PRiCE, 1990; Carlson et al., 1995; Gillies et al., 1997; Jiang and Islam, 2001; Sandholt et al., 2002; Nishida et al., 2003; Long and Singh, 2012; Merlin et al., 2014; Yang et al., 2015; Minacapilli et al., 2016).

EB- and EF-based ET models have been extensively and successfully applied in relatively flat regions. However, their implementation in mountainous areas presents a significant challenge due to the complex interplay of topography, vegetation, and meteorological factors. This complexity arises from small-scale variations in elevation, slope, and aspect, which greatly influence local meteorological forcing, vegetation and soil properties (Nippgen et al., 2011). For instance, air temperature (Ta) and precipitation vary with elevation, and incoming shortwave radiation (Rg) is affected by the surface's topographic geometry (Pepin et al., 2015; Malbéteau et al., 2017; Hao et al., 2021). Additionally, the diverse vegetation types and soil conditions present within mountainous regions add to the heterogeneity of those landscapes (Tague et al., 2009). Such a variability in surface and meteorological conditions (induced by topography) poses challenges for a generic usage of these ET models.

To accurately estimate ET in mountainous regions and evaluate the performance of EB- and EF-based models, it is imperative to account for topography and its impact on meteorological and surface conditions. On the one hand, EB-based models require high-resolution meteorological forcing and input parameters. The point is that the spatialization of meteorological and surface variables in mountain is a difficult task (Terzago et al., 2020; Evin et al., 2024), and given the uncertainties associated with these input data at high spatial resolution, the relevance of EB-based models in such complex landscapes has yet to be demonstrated. On the other hand, EF-based models are known for requiring fewer input variables and for being less sensitive to errors in meteorological variables compared to EB-based models (Majozi et al., 2017; Chen and Liu, 2020). Nevertheless, EF-based models rely on the assumption that meteorological forcing is uniform across the study area (Stisen et al., 2008), which is absolutely not the case in mountainous regions (de Tomás et al., 2014). Therefore, the applicability of the EF-based approach in these environments requires a prior normalization procedure to account for topography-induced variations in the remotely sensed LST (Hais and Kučera, 2009; Malbéteau et al., 2017; Firozjaei et al., 2020).

To date, a limited number of studies have applied thermal-based ET models in mountainous regions. Table 1 provides a summary of the key papers found in literature. Four different EB-based models have been utilized: Gao et al. (2011) employed the SEBTA model, incorporating specific adjustments for solar exposure and elevation to account for topographical influences on ET estimation. Castelli et al. (2018) investigated the ALEXI/DisALEXI model's performance, focusing on flux disaggregation without implementing topographic corrections. Han et al. (2021) adopted the SEBS model, integrating algorithms designed to address subgrid-scale topographical variations. Guzinski et al. (2021) used the TSEB and ET-Look models, incorporating elevation and exposure-based corrections. Conversely, the EF-based models have been applied in two distinct studies. Zhao and Liu (2014) utilized the surface-air temperature difference versus the VI space (LST-Ta)-VI, with cosine adjustments for LST and albedo. More recently, Zhu et al. (2023) enhanced ET estimations by employing the LST-VI model with a modified temperature vegetation dryness index at a pixel scale, considering solar exposure.

A common limitation among these studies is the use of low (1 km or lower) resolution LST data as input, which does not reflect the great variability of mountain surface conditions. More fundamentally, while most of these studies have incorporated terrain corrections, no quantitative evaluation was proposed to assess the performance of such corrections on ET estimates at the LST data resolution (Castelli et al., 2018; Han et al., 2021; Guzinski et al., 2021). The lack of validation strategy at the scale of topographic effects was due to either the unavailability of in situ measurements as in the case of Zhao and Liu (2014) and Zhu et al. (2023), or the unavailability of monitoring stations located at different elevations (Gao et al., 2011). Consequently, the topography-induced variability of meteorological and surface conditions, and its impact on ET estimates remains largely underexplored across mountainous regions. In addition, there has also been no comprehensive intercomparison of EB- and EF-based models on areas with a pronounced topography. Such a comparison would be particularly useful in assessing the relative impact of meteorological forcing uncertainties on each of the two ET modeling approaches.

In this context, the aim of this study is to adapt, evaluate, and compare the ability of two EB- and EF-based ET modeling approaches at fine resolution in a steep-sided watershed. Input data notably include 30 m resolution Landsat visible/near-infrared, thermal-based LST data (resampled at 30 m), and meteorological data including Rg, Ta, wind speed (Ws), and air relative humidity (Rh). The Priestley-Taylor version of the Two Source Energy Balance model (TSEB-PT) is used as the EB-based approach, and the LST-VI model is used as the EF-based approach. Both models are implemented over a 20 km by 44 km area in the High Atlas mountain range for the period 2020–2022. The evaluation is based on measurements collected from six automatic weather stations (AWS) at varying elevations and two EC towers positioned at different elevations: one at 900 m above sea level (m.a.s.l.) at the foothills and the other at 3850 m.a.s.l., the highest flux station in North Africa.

First, meteorological data are spatialized at the Landsat spatial resolution using disaggregation, modeling, and resampling techniques. Then, the LE estimated by TSEB-PT and LST-VI models, with or without considering topographic effects, is assessed against localized EC measurements. Finally, a regional-scale analysis is carried out to compare the spatial distribution of LE and EF derived by both models, providing a comprehensive evaluation of their performance in accounting for topographical effects.

Table 1
Summary of studies implementing thermal-based ET models in mountainous regions.

Study	ET model	Spatial resolution of LST data	Spatial resolution of meteorological data	Topographical corrections of meteorological/surface conditions	Validation strategy	Quantitative evaluation (in W/m2 and/or %) of the impact of topography on ET and/or EF retrieval (with/ without topographical corrections)
Gao et al. (2011)	Surface Energy Balance with Topography and Land-cover Effects (SEBTA)	1 km	1 km	A shading coefficient is applied to the solar radiation estimated by taking into account solar exposure. LST is corrected for elevation by using a constant lapse rate (−6.5 °C/km) relative to the mean elevation of the study area.	Comparison with lysimeter and EC data at a single site (28 m.a.s.l.).	No evaluation
Zhao and Liu (2014)	(LST-Ta)-VI	1 km resized to 250 (nearest-neighbor)	5 km resized to 250 (nearest-neighbor)	Cosine correction to LST and albedo.	Comparison against ET estimates derived from the water balance at sub-basin (over 1500 m.a.s.l.) and annual scales.	The average relative error of the retrieved ET is 18.0 % and − 7.1 % before and after topographic correction, respectively.
Castelli et al. (2018)	Two Source Energy Balance Atmosphere Land EXchange Inverse (ALEXI/ DisALEXI)	3.5 km (ALEXI) 1 Km (DisALEXI)	3 Km	No topographical correction.	Comparison with EC data at two sites (elevation information not provided) located 500 m apart (irrigated meadow and rainfed pasture), and with TSEB simulations applied to local meteorological data and considered as benchmark.	No evaluation
Han et al. (2021)	Surface Energy Balance System (SEBS)	1 km (remapped onto 10 Km grid)	~10 Km	The form drag caused by the subgrid-scale topographical obstacles is taken into account in SEBS.	Comparison with EC data at six sites (3326, 3668, 4264, 4276, 4509, 4730 m.a.s.l.).	No evaluation
Guzinski et al. (2021)	TSEB /ET-Look	1 km sharpened to 300 m and bilinearly interpolated to 100 m and 20 m	30 km spatialized to 300 m and bilinearly interpolated to 100 m and 20 m	Ta and dew temperatures are spatialized using a standard lapse rate value (of −6.5 and − 2 °C/km, respectively). Solar radiation is corrected for elevation and solar exposure.	Comparison with EC and lysimeter data at six sites (elevation information not provided).	No evaluation
Zhu et al. (2023)	LST-VI applied at pixel scale	1 km	1 km	Solar radiation takes into account solar exposure.	Comparison to other remote sensing-based (GLEAM, SSebop, ET_Ma, and GRACE-derived ET) ET products.	No evaluation

2. Study area and data

2.1. Study site

The 860 km2 study area is located in the High Atlas mountain range in Morocco, approximately 40 km south of Marrakech city (Fig. 1). It includes the 225 km^2 Rheraya catchment, which constitutes a segment of the Tensift watershed and displays a diverse array of elevations, extending from 1060 m.a.s.l. at its lowest point to the zenith of North Africa's highest mountain, Mount Toubkal, at 4167 m.a.s.l. (Chaponnière et al., 2008). Geological features within the Rheraya catchment entail sedimentary formations within the northern foothills and magmatic rock structures in the southern elevated mountainous regions. These elevated areas exhibit cool temperatures and limited vegetation cover, in contrast to the river valleys where most agricultural activities are concentrated (Simonneaux et al., 2015). The land use in the region includes degraded rangelands on mountain slopes with sparse chamaephyte cover due to overgrazing, cedar woodlands located on the northern foothills with higher precipitation levels, irrigated crops around the primary hydrological network (comprising 5 % of the total area), and dry crops on some gentle limestone slopes to the north of the watershed (Simonneaux et al., 2015).

Since 1989, the Rheraya catchment has been monitored for hydrologic characteristics. In the framework of the SUDMED program (Chehbouni et al., 2008) and Joint International Laboratory LMI-TREMA (Jarlan et al., 2015) activities, the Tensift Observatory has established two EC flux towers and multiple AWS within the area (Fig. 1). One of the AWS (Aremd at 1940 m.a.s.l.) had recorded during the 2003–2006 period an average Penman-Monteith reference ET value of 1073 mm per year. Precipitation levels within the catchment exhibit considerable variability, with annual rates ranging between 300 and 700 mm, depending on site location. The watershed's average precipitation is estimated to be approximately 490 mm, with one-third of this amount falling as snow and a minimum monthly rainfall rate typically reached between June and September (Cheggour et al., 2008; Simonneaux et al., 2015).

2.2. Ground-based measurements

The two sites (Tazaghart and Tahanaout, ref. to Fig. 1) equipped with

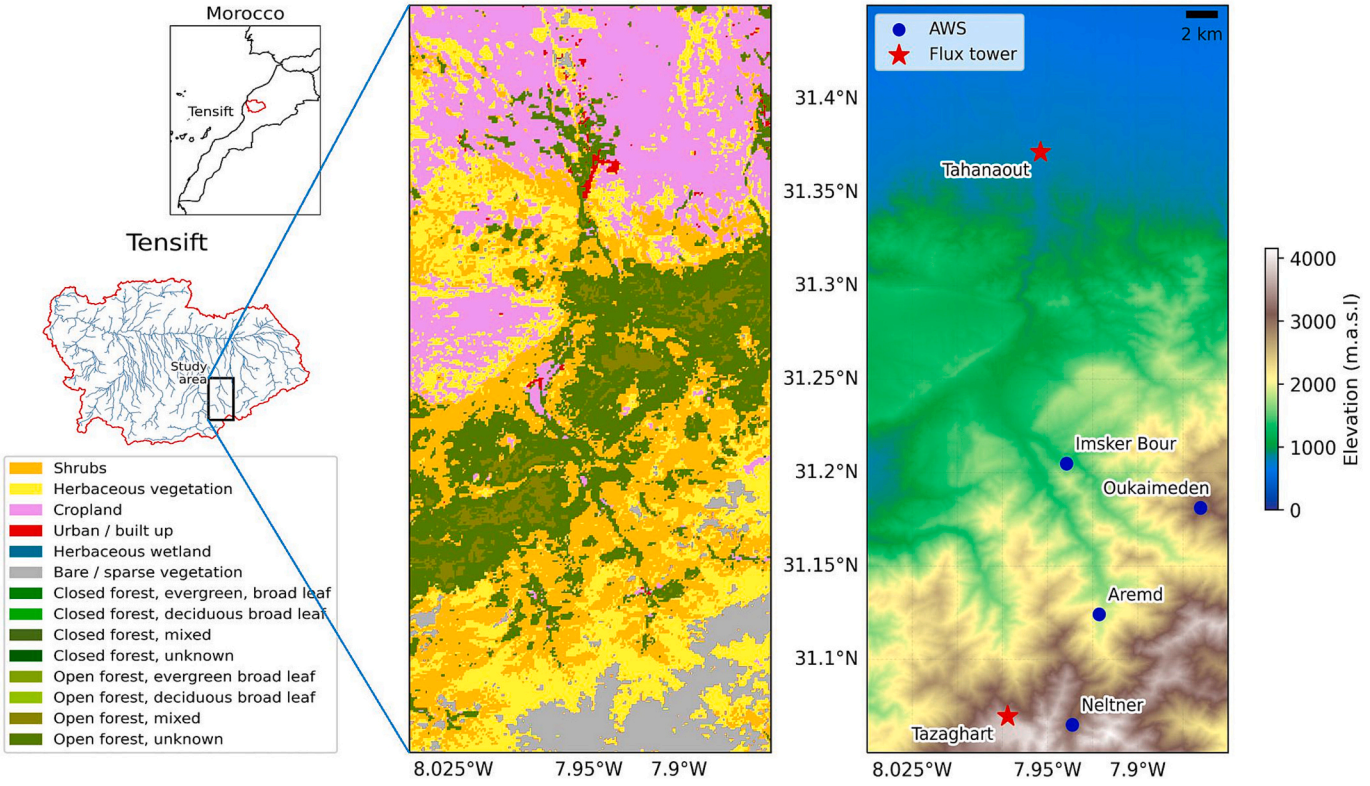

Fig. 1. Study area's location (left), land-cover map (middle), and topographic map (right).

the EC system have distinct geographic characteristics. The Tazaghart tower is positioned on a high plateau, approximately 3850 m.a.s.l., with mainly black rocks and an underlying silty-clay soil. Vegetation is absent for most of the year within a radius of at least 200 m. At the southern end of the Haouz plain, the Tahanaout tower is situated in a foothill site. It is positioned at the outlet of the Rheraya and is approximately 900 m.a.s.l. The area is mainly occupied by traditional agriculture that primarily relies on the water of Rheraya. Land use comprises mainly a combination of trees (olives) and annual crops (cereals).

Both sites are equipped with sensors that measure flux and meteorological variables. These include LE (Campbell Scientific Ltd. KH20), H (Campbell Scientific Ltd. CSAT3), net radiation's (Rn) four components (Campbell Scientific Ltd. CNR4), and G, the ground heat flux (Campbell Scientific Ltd. HPF01, with heat plates positioned at the vicinity of the towers). The Tazaghart EC tower's equipment is located at an approximate height of 2 m above ground level (a.g.l.), while at Tahanaout, it is positioned at a height of about 17.6 m a.g.l. Average fluxes over 30 min measured by the flux stations (LE, H, Rn and G) from 2020 to 2022 were used to evaluate the performance of ET models. At Landsat overpass times, the mean EB closure calculated is about 90 % and 70 % for Tazaghart and Tahanaout sites, respectively. To ensure EB closure, any residual energy imbalance was allocated to the LE flux. This decision was based on the recognition that measuring LE accurately poses greater challenges in terms of humidity sensor calibration compared to the measurement of H using temperature sensors (Foken et al., 2011; Guzinski et al., 2020). The Flux tower's footprint analyses were conducted using a Python script based on the Flux Footprint Prediction (FFP) model, available at http://footprint.kljun.net/ (last accessed 15/10/2023). This model, developed by Kljun et al. in 2015 (Kljun et al., 2015), represents a prominent Lagrangian statistical technique for estimating tower-based source areas. Its accuracy and ease of use have been well-established in the field (e.g., Chu et al., 2021; Mbabazi et al., 2023; Volk et al., 2023).

Meteorological data are collected from six AWS positioned at different elevations (Fig. 1). In addition to Tahanaout and Tazaghart, the AWS sites include Imskerbour (1404 m.a.s.l.), Aremd (1940 m.a.s.l.), Neltner (3207 m.a.s.l.), and Oukaimden (3207 m.a.s.l.). These AWS exhibit variability in instrumentation configurations, with certain stations capturing only a subset of the five meteorological variables. For this study, the ground AWS measurements were not used as input to ET models. They solely contributed to calibrating and/or validating spatialized high-resolution meteorological data. A more detailed description of both towers and AWS network locations and set-up can be found at https://www.lmi-trema.ma/, last accessed 03/10/2023.

2.3. DEM data

The Shuttle Radar Topography Mission's (SRTM) 1 arc *sec* DEM is used here as the primary topographic dataset. Developed collaboratively by the NASA Jet Propulsion Laboratory and the National Geospatial-Intelligence Agency, the SRTM's 1 arc sec DEM provides a high-resolution spatial representation with an approximate 30 m resolution, encompassing global coverage (freely available at: https://earthexplorer.usgs.gov/ last accessed on 03/10/2023). Its main objective in the study is to account for topographic effects on LST and meteorological data, focusing particularly on the impact of elevation and sun exposure. To this end, two specific SRTM 1 Arc-Second tiles (SRTM1N31W008V3 and SRTM1N31W009V3) were mosaicked, gap filled to generate a 30 m resolution DEM subset over the study area (Fig. 1).

2.4. High-resolution meteorological data

2.4.1. Ta, Rh and Ws data

The state-of-the-art ERA5-Land reanalysis provides a comprehensive global dataset for land applications (Muñoz-Sabater et al., 2021). It is generated by the European Centre for Medium-Range Weather Forecasts (ECMWF) and produces a total of 50 variables at 9 km spatial resolution on an hourly timestep. Notably, three products included in this dataset are used in this study: 2 m Ta (t2m), 2 m dew point temperature (d2m),

and 10 m horizontal Ws of air moving towards the east and north (U10 and V10, respectively). The ERA5-Land Ta, Rh, and Ws data are spatially distributed at 30 m resolution across the study area based on the procedure described in the following.

The influence of elevation on Ta is addressed through a disaggregation approach at 30 m resolution of 9 km resolution ERA5-Land t2m data (Sebbar et al., 2023). This methodological choice represents a substantial advance over traditional downscaling methods, such as the use of the global mean ELR typically set at -6.5 °C.km^{-1} or the MicroMet model (Liston and Elder, 2006). It also has the advantage of already being specifically calibrated within the Rheraya catchment, which is included in the study area of this study. The methodology in Sebbar et al. (2023) comprises three main steps:

1. The ERA5-Land t2m data at the 9 km spatial resolution is adjusted (at its native resolution) to remove any persistent bias against in-situ measurements. This adjustment is performed using an XGBoost model (Chen and Guestrin, 2015) that was trained over the basin using hourly ground observations collected over five years (2016 to 2020). The model's dependent variables include hourly ERA5-Land t2m and corresponding ELR, daily mean and daily standard deviation of t2m values, and ERA5-Land DEM data. This process results in corrected t2m values for the area, referred to as t2m_corr.
2. The ELR is updated at 9 km resolution based on the previously corrected t2m_corr data, effectively capturing the complex relationship between Ta and elevation in real time.
3. The t2m_corr data, corrected at a 9 km resolution, are then downscaled to the finer resolution of 30 m using SRTM's DEM. This disaggregation follows the equation:

$$Ta_{30m} = t2m\_corr_{9\ km} + ELR_{9\ km}(DEM_{30\ m} - DEM_{9\ km})$$

Here, $ELR_{9\ km}$ represents the updated ELR, $DEM_{30\ m}$ is the 30 m resolution DEM from SRTM, and $DEM_{9\ km}$ is DEM at ERA5-Land resolution.

Rh is spatialized at 30 m resolution from the downscaled d2m (Tdew) and Ta data. ERA5-Land d2m data are disaggregated using the same approach as for Ta described above, where the temperatures are Tdew, and the ELR is the dew point temperature lapse rate. Note that the direct use of the ELR method may result in errors, especially in regions where humidity fluctuates dramatically. However, in this study, by incorporating real conditions through model training, the aim is to reduce errors as much as possible when downscaling Tdew using this ground-informed disaggregation ELR method. Vapor pressure (e_{act}) is computed using the Magnus-Tetens formula (Magnus, 1844; Monteith and Unsworth, 2013) expressed as: $e_{act} = 0.61078 \times e^{\frac{17.27T_{dew}}{T_{dew}+237.3}}$. Similarly, the saturation vapor pressure (e_{sat}) is estimated using the same formula, but with 30 m resolution downscaled Ta as the input variable: $e_{sat} = 0.61078 \times e^{\frac{17.27T_a}{T_a+237.3}}$. Both e_{act} and e_{sat} are in kPa, while Ta and Tdew are in °C. Finally, the 30 m resolution Rh is estimated as $Rh = 100 \times \frac{e_{act}}{e_{sat}}$.

There is currently no widely accepted and satisfactory model that fully accounts for the complex topographical effects on Ws. Existing models and tools, constrained by simplifications and assumptions, are unable to fully account for the complex dynamics of Ws or are impractical for regional runs (e.g., measurement strategy unmanned aerial vehicle (UAV) outlined by Ingenhorst et al., 2021 (Ingenhorst et al., 2021)). Therefore, ERA5-Land derived Ws data are simply resampled to 30 m resolution using the bilinear interpolation approach.

Note that other ancillary meteorological data such as barometric pressure, air density or air heat capacity are needed as input to ET models. Those variables are thus distributed spatially either by using the 30 m resolution DEM data directly, or from the downscaled Ta dataset that integrates the high-resolution DEM information.

2.4.2. Rg data

The complex interactions between mountainous terrains and Rg pose challenges for accurately capturing and representing this relationship in reanalysis such as ERA5-Land datasets. In this study, the 30 m resolution Rg maps are instead simulated by considering three different components: direct solar radiation (Rg_{dir}), diffuse solar radiation (Rg_{diff}), and the solar radiation (Rg_{adj}) reflected from adjacent surfaces. The direct component is estimated proportionally with the cosine of the solar incidence angle using the semi-empirical model developed by Samani et al. (2007):

$$Rg_{dir} = G_{sc} cos\theta d_r \tau_{sw} \quad (1)$$

With G_{sc} being the solar constant (1367 W/m^2), θ the solar incidence angle determined from the metadata of Landsat images, d_r the inverse relative earth-sun distance, and τ_{sw} the atmospheric transmissivity. The formula for calculating d_r is provided by Allen et al. (1998) and involves the Julian day of the year (J) as expressed by the equation $d_r = 1 + 0.033cos\frac{2\pi J}{365}$. The equation for deriving τ_{sw} is also proposed by Allen et al. (1998) and utilizes the DEM as follows: $\tau_{sw} = 0.75 + 2 \times 10^{-5}(\text{DEM})$.

The diffuse component of Rg is approximated using a quadratic function with Rg_{dir} as the input. Likewise, the adjacent component Rg_{adj} is represented as a linear function of elevation. These parametric functions recenter the errors relative to simulations from DART (Discrete Anisotropic Radiative Transfer), a three-dimensional radiative transfer model (Gastellu-Etchegorry et al., 2004) used as a reference in this study. DART is widely regarded as one of the most complete models for simulating the radiative transfer in heterogeneous three-dimensional landscapes using advanced kernel and discrete ordinate methods. It should be noted that the direct implementation of DART at the scale of the study area was not pursued due to its extensive computational requirements. Generating a single Rg map requires considerable time and resources. Instead, DART is used herein as a benchmark for assessing the semi-empirical Rg model on a subset of the study area.

2.5. Remote sensing data

2.5.1. Landsat data

The primary source of remote sensing reflectance and thermal infrared observations used in this study for ET modeling comes from the latest Collection 2 Level 2 (C2L2) products of Landsat-7, Landsat-8, and Landsat-9 satellites. Generated by the USGS Earth Resources Observation and Science (EROS) Center, these products offer key characteristics that make them an excellent source of atmospherically corrected information for remote sensing applications. The thermal infrared bands, originally captured at 100 m resolution for Landsat-8 and Landsat-9 and 60 m for Landsat-7, are resampled to a 30 m resolution in the final C2L2 products. Additionally, the enhanced vertical accuracy from multiple DEM sources within the Landsat Collection 2 DEM improves the overall quality of the data, especially in mountainous regions (Franks et al., 2020). Vegetation indices are calculated from the top-of-canopy reflectance bands and Landsat LST is derived from the thermal band as described in Landsat 4–7 and Landsat 8–9 Collection 2 (C2) Level 2 Science Product (L2SP) Guides.

For the EB-based ET approach, the 30-m resolution LAI product used in this study is computed as $= \sqrt{\left(NDVI\frac{1+NDVI}{1-NDVI}\right)}$, based on Landsat NDVI following Wang et al. (2008). The fraction of vegetation that is green and actively transpiring (fg) is derived using NDVI and Enhanced Vegetation Index (EVI). For most land cover classes, fg is estimated according to the approach stated in Guzinski et al. (2013), whereby $fg = 1.2\frac{EVI}{NDVI}$ $(0 < fg < 1)$. For croplands, a distinct approach is applied to fg, which is set to be equal to EVI solely during the crop senescence period (occurring between day-of-year 160 and 230), and as 1 during other time periods (Guzinski et al., 2013).The fractional vegetation cover (fc) is estimated as a non-linear function of LAI based on the Beer-Lambert

law (e.g., Trebs et al., 2021) as $fc = 1 - e^{\left(\frac{-k\,LAI}{cos(vza)}\right)}$, with K being the attenuation coefficient of Rg within the canopy that depends on the land-cover type of the pixel, and vza standing for the satellite's viewing zenith angle.

For the EF-based ET approach, fc is derived directly from NDVI and used as the VI for constructing the LST-VI feature space. As a first-order estimate, Gutman and Ignatov (1998) proposed $fc = \frac{NDVI - NDVIs}{NDVIv - NDVIs}$, where NDVIs and NDVIv corresponds to bare soil and full vegetation cover respectively. Due to our adherence to the original formulas and methodologies employed in the works we are building upon. The choice of using two different fc formulas is primarily due to adherence to the original formulas and methodologies employed in the foundational works that this study builds upon to ensure consistency and methodological integrity. Note that during the study period (2020–2022), Landsat observations over the study site were available on 38 dates.

2.5.2. Land-cover data

Besides the information obtained from satellite observations, running ET models on a regional scale requires additional spatially distributed data like vegetation height and average leaf size. Such variables can be derived from a land-cover map which, in conjunction with empirical models and look-up conversion tables (e.g., Table.1 in Guzinski and Nieto, 2019, Table.2 in Guzinski et al., 2020, and Tables A1–A5 in Floors et al., 2021) assigns input surface parameters that cannot be directly estimated from satellite observations (Schaudt and Dickinson, 2000).

The 2019 version of the Copernicus Global Land Service's Land Cover 100 m resolution product is used as the primary data source for generating a land cover map for each satellite over-pass date. The dataset offers comprehensive global coverage, obtainable from the Copernicus Land Monitoring Service (http://land.copernicus.eu, accessed on 15/10/2023). To prepare the land cover map for high-resolution model runs, it is regrouped to a smaller number of classes and resampled from its original 100 m resolution to 30 m resolution. Furthermore, to ensure a more up-to-date representation of herbaceous classes heights, which have a substantial impact on aerodynamic roughness (Raupach, 1994; Schaudt and Dickinson, 2000; Guzinski et al., 2020), a power law scaling method is employed, following the approach described in Guzinski et al. (2020). This method considered both the Plant Area Index $\left(PAI = \frac{LAI}{f_g}\right)$, and the maximum vegetation height indicated in Table 2. The minimum value for the scaled vegetation height was set to one tenth of the maximum value.

Additional ancillary parameters are also shown in Table 2: the f_{Clump} represents the portion of ground covered by a clumped canopy ($f_{Clump} = 1$ indicates a homogenous canopy). The w_c/h_c parameter represents the canopy width to canopy height ratio, the average leaf size (l_w), and the Campbell's leaf angle distribution (χ) parameter (Campbell, 1986). Aerodynamic roughness length for momentum transfer and zero-plane-displacement height were estimated using canopy heights and land cover type based on the Raupach formulations (Raupach, 1994; Schaudt and Dickinson, 2000).

Table 2
Ancillary parameters derived from land cover classes in the study area. CGLS land cover legend can be found in the product user manual provided by Buchhorn et al. (2020).

CGLS_LC code	$h_{c,\,max}$ (m)	PAI_{max} (–)	f_{clump} (–)	w_c/h_c (–)	l_w (m)	χ
20	2	2	0.15	1	0.05	1
30	1	5	1	1	0.02	0.5
40	1.2	5	1	1	0.02	0.5
50	20	0	0	0	0	0
60	0	0	0	0	0	0
90	1	5	1	1	0.02	0.5
112	10	5	1	1	0.15	1
114	10	5	1	1	0.15	1
115	15	5	1	1.5	0.1	1
116	15	5	1	1.5	0.1	1
122	10	5	1	1	0.15	1
124	10	5	1	1	0.15	1
125	15	5	1	1.5	0.1	1
126	10	5	1	1	0.15	1

3. ET models

The flowchart in Fig. 2 provides a graphical representation of the overall methodological approach adopted in this paper. The EB-based and EF-based ET estimation approaches are presented separately in this section.

3.1. EB-based ET model

To analyze the surface EB from a physically-based perspective, TSEB-PT model is used in this study. It is an enhanced version of the TSEB model, which builds upon the original model proposed by Norman et al. (1995) and further improved by Kustas and Norman (1999). TSEB-PT decomposes the directional radiometric LST into distinct components for vegetation and soil. This division enables the independent estimation of Rn, LE and H for each component. The estimated fluxes are then integrated to determine bulk surface fluxes.

To facilitate the complex heat transfer between these components and the surrounding atmosphere, the model incorporates resistances that emulate the behavior of electrical systems. These resistances depend on aerodynamic and meteorological conditions and play an essential role in regulating the interaction of the turbulent fluxes originating from vegetation and soil. A fundamental aspect of the modeling process is the iterative computation of canopy temperature and soil temperature, since these variables are not known at the outset. The core of the TSEB-PT model is based on the assumption of a canopy potential transpiration rate, derived from the Priestley-Taylor formula (Priestley and Taylor, 1972):

$$LE_c = \alpha_{PT} f_g \frac{\Delta}{\Delta + \gamma} R_{n,c} \tag{2}$$

where α_{PT} is the Priestley-Taylor coefficient (initially set to its default value of 1.26), Δ the slope of the vapor pressure to Ta curve, γ the psychrometric constant, and $R_{n,c}$ denotes the canopy net radiation.

In this study, the partitioning of Rn into soil and canopy components is carried out by considering both shortwave and longwave radiations from soil and canopy. Shortwave net radiation was modeled using the approach proposed by Kustas and Norman (1999) driven by the 30 m resolution Rg. The longwave radiation emitted by the land surface was calculated using the Stefan-Boltzmann equation, which takes into account the LST and emissivity. Finally, the atmospheric irradiance absorbed by the surface is calculated on the basis of Kirchhoff's law, using 30 m resolution Ta, surface emissivity and atmospheric emissivity data. Note that for barren pixels, the EB equation is solved as single source using the one-source EB-based model instead of TSEB-PT. In this case, no canopy/soil partitioning is required, Rn is calculated as in Malbéteau et al. (2017) (Eq. A.2), and the LST is used to calculate ET as follows (Bartholic et al., 1972; Brown, 1975; Stone and Horton, 1974; Heilman et al., 1976; Clothier et al., 1986; Kustas and Daughtry, 1990; Sandholt and Andersen, 1993; Chen and Liu, 2020):

$$\mathrm{ET} = R_n - G - \rho c_p \frac{LST - T_a}{r_a} \tag{3}$$

Where ρ stands for the density of air, c_p refers to the air's specific heat, while r_a denotes the total aerodynamic resistance, which is the aggregate of the fundamental aerodynamic resistance and the excess

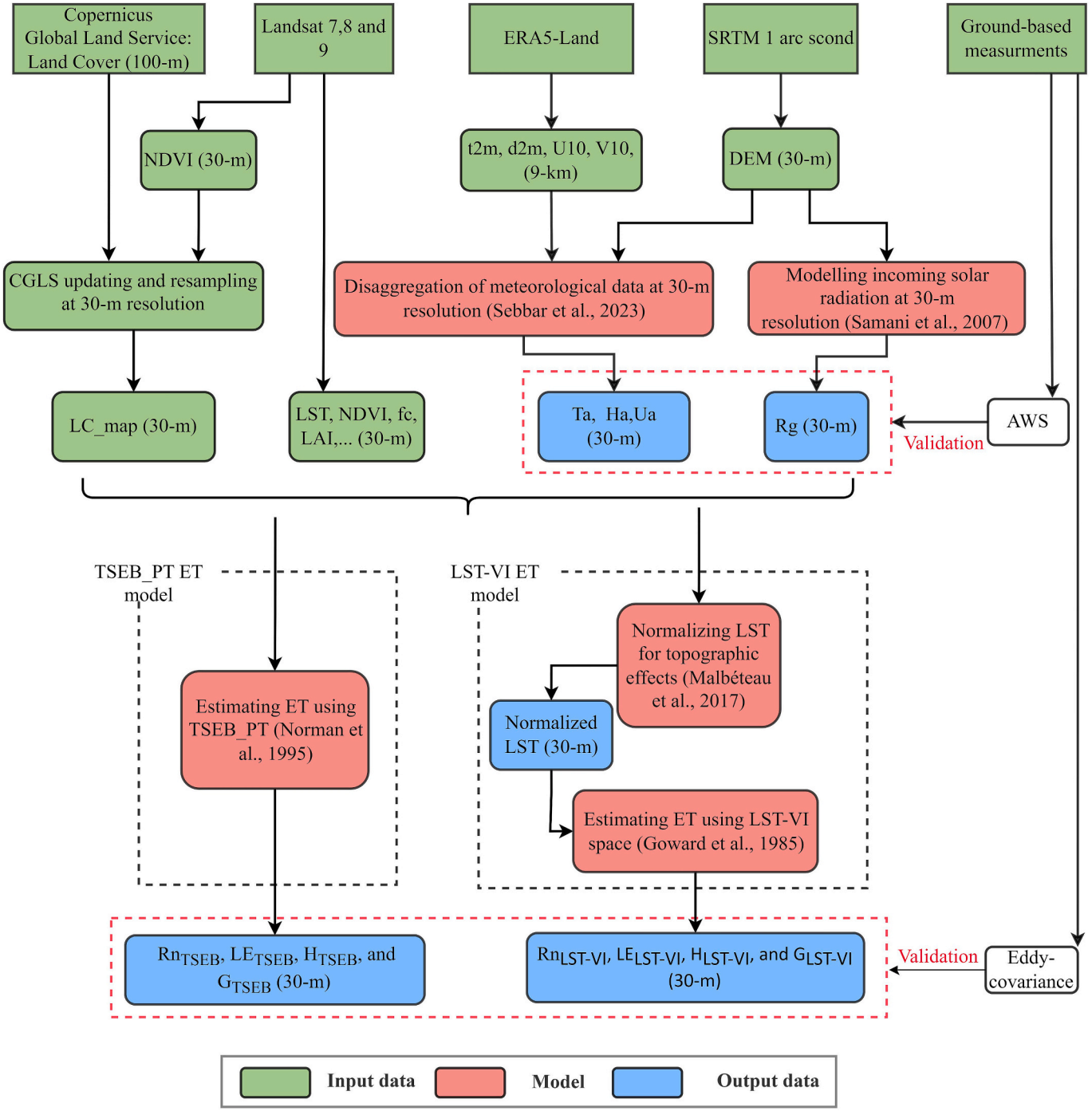

Fig. 2. Flowchart of the input/output data and the different models used to implement and evaluate two (EB- and EF-based) high-resolution ET estimation approaches in mountainous areas.

resistance (Eq. 2, Chen and Liu, 2020). The excess resistance component is crucial as it compensates for the differences between the remotely sensed LST and the aerodynamic canopy temperature. Several variables were considered for the partitioning between soil and vegetation components, namely LAI, χ, bi-hemispherical reflectance and transmittance for the soil and a single leaf, and f_{clump} (for dealing with heterogeneous canopies). In line with previous studies, the current investigation adopts a series configuration of resistances (e.g., Morillas et al., 2013; and Guzinski and Nieto, 2019). Moreover, G is approximated as a percentage of Rn, depending on whether it is a high canopy, a short canopy, or bare soil using the methodology proposed in GLEAM by Miralles et al. (2011).

For a more detailed understanding of TSEB-PT model and its implementation, the complete source code of Python implementation is publicly available online (https://github.com/hectornieto/pyTSEB/releases/tag/v1.4, last accessed on 03/10/2023), as well as the cited publications that thoroughly describe the TSEB model and its adaptations.

3.2. EF-based ET model

3.2.1. EF formulation

The acquisition of regional-scale meteorological measurements and the accurate estimation of aerodynamic temperature and resistance for H calculations are common issues. To overcome these challenges,

numerous models have been developed to exploit the spatial contextual information provided by remotely sensed LST data in areas characterized by a wide range of vegetation fractions. These models estimate EF, which is used to calculate LE, taking into account the energy available at the surface (Goward et al., 1985; PRiCE, 1990; Merlin et al., 2008; Merlin, 2013; Chen and Liu, 2020).

Briefly, using the EF-based ET models, also referred to the triangle/trapezoidal method due to the shape formed by the LST-VI scatter plot, LE can be estimated as follows (Jiang and Islam, 1999; Chen and Liu, 2020):

$$LE = \mathrm{EF}(R_n - G) = \phi\left[(R_n - G)\frac{\Delta}{\Delta + \gamma}\right] \quad (4)$$

where ϕ can be interpreted as an equivalent to α_{PT} (Priestley and Taylor, 1972). ϕ reaches a maximum value (ϕ_{max}) of 1.26, and for a pixel i, a minimum value ($\phi_{min,i}$) that can be approximated by fc$\times\phi_{max}$ (Chen and Liu, 2020). For a point i in the LST-VI space, EF can be expressed as follow:

$$\phi = \frac{LST_{max} - LST_i}{LST_{max} - LST_{min}}\left(\phi_{max} - \phi_{min,i}\right) + \phi_{min,i} \quad (5)$$

Where LST_{max} and LST_{min} represent, for a given pixel i, the corresponding LST on the dry edge and the corresponding LST on wet edge, respectively. The dry edge refers to conditions with the highest possible LST and the lowest ET rate for a given fc, while the wet edge corresponds to conditions where the EF is at its maximum.

Determining the value of ϕ, by interpolating the relative position of each point within the LST-VI space between the dry and wet edges, highlights the importance of exercising when determining these edges, although the contextual approach is generally perceived as straightforward. The dry and wet edges estimation is particularly challenging in mountains as the landscape is characterized by steep-sided valleys and significant elevation gradients, where the wet edge is likely to be influenced by distortions caused by the variability of Ta and shadowed slopes with low LST values.

3.2.2. Normalizing LST for topographic effects

One way of addressing the impact of topography (notably slope exposure and elevation effects) on the determination of wet/dry edges in EF-based ET models is through the normalization of LST data for topography-induced variability of the atmospheric forcing. This technique involves a systematic removal of the topographic effects from the remotely sensed LST values, enabling them to exhibit behavior within the LST-VI space consistent with that observed in uniformly flat areas. As a result, it would be possible to retrieve EF values regardless of topographic influence, and eventually estimate ET, as is commonly done over flat areas.

The adopted LST normalization technique was developed by Malbéteau et al. (2017). This method stands out as a remarkable advancement in the state-of-the-art of LST topographic normalization through a physically-based soil and vegetation EB inversion. The normalization model is written as:

$$LST_{norm} = LST_{Landsat} - LST_{EB}(Rg, E) + LST_{EB}(\langle Rg\rangle, \langle E\rangle) \quad (6)$$

Where $\mathrm{LST_{norm}}$ represents the Landsat LST normalized for topographic effects using the Malbéteau et al. (2017) approach and $LST_{Landsat}$ the observed Landsat LST. $LST_{EB}(Rg, E)$ represents the LST simulated via the EB solving, using pixel-scale elevation and Rg. $LST_{EB}(\langle Rg\rangle, \langle E\rangle)$ refers to the LST simulated by the EB equations using the average values of elevation and Rg at the scale of the study area. LST is estimated as a linear function of component temperatures, as described in studies by Merlin and Chehbouni (2004), Anderson et al. (2008), Long and Singh (2012), and Malbéteau et al. (2017):

$$LST_{EB} = f_c \times T_{s_{EB}} + (1 - f_c) \times T_{v_{EB}} \quad (7)$$

$$T_{v_{EB}} = f_{sv} \times T_{v,dry_{EB}} + (1 - f_{sv}) \times T_{v,wet_{EB}} \quad (8)$$

$$T_{s_{EB}} = f_{ss} \times T_{s,dry_{EB}} + (1 - f_{ss}) \times T_{s,wet_{EB}} \quad (9)$$

with $T_{s_{EB}}$ being the simulated soil temperature, f_{ss} a dryness index of the soil surface (f_{ss} equals to 1 when the soil is fully dry and to 0 when the soil is fully wet), $T_{v_{EB}}$ the simulated vegetation temperature, f_{sv} a vegetation water stress index (f_{sv} is equal to 1 when the root zone soil moisture is above field capacity and to 0 when the root zone soil moisture is below the wilting point) and $T_{v,dry_{EB}}$, $T_{v,wet_{EB}}$, $T_{s,dry_{EB}}$, and $T_{s,wet_{EB}}$ the simulated temperature of fully stressed vegetation, unstressed vegetation, dry soil, and wet soil respectively. The four simulated temperature endmembers ($T_{v,dry_{EB}}$, $T_{v,wet_{EB}}$, $T_{s,dry_{EB}}$, and $T_{s,wet_{EB}}$) and the simulated component temperatures ($T_{s_{EB}}$, $T_{v_{EB}}$) are estimated by solving the EB numerically using Newton's method (Bristow, 1987).

The LST normalization approach of Malbéteau et al. (2017) is parameterized as a function of three parameters: f_{ss} and f_{sv} in Eq. (8) and (9) and ELR, which is used to spatialize Ta at the Landsat resolution within the study area. The method initializes the ELR with a first-guess value of -6 °C.km^{-1}, and then iterates on adjusted ELR values for inverting both f_{ss} and f_{sv} parameters by minimizing the RMSE difference between simulated and observed LST. In this study, ELR is estimated independently from the method in Sebbar et al. (2023), so that only f_{ss} and f_{sv} parameters are inverted from the LST normalization approach. Note that f_{ss} and f_{sv}, as well as the temperature endmembers are defined at the scale of the study area in Malbéteau et al. (2017). For a thorough understanding of the EB-based topographic normalization process, including detailed equations and explanations, readers are encouraged to refer to the work of Malbéteau et al. (2017).

Note that, to avoid any confusion, we clarify that the normalized LST is not used as input to TSEB-PT. The TSEB-PT model operates on a pixel-by-pixel basis. Each pixel is treated as an isolated piece of land, and the inputs are iterated until energy balance convergence is achieved. This approach makes it unnecessary and irrelevant to normalize the LST in the TSEB-PT model. In contrast, the influence of topography is accounted for using meteorological variables spatialized at the operating scale of TSEB-PT.

3.2.3. Consolidating the dry edge determination

Remaining pixels outside the designated polygon in the LST-VI space can lead to overestimation of the dry edge or underestimation of the wet edge. These outliers could potentially be attributed to a combination of factors, including uncertainties in the fine-scale meteorological forcing, uncertainties in the DEM and micro-topography at the sub-pixel scale DEM. To make the determination of the dry edge more robust (than relying on the EB-simulated temperature endmembers) and to remove outliers, Tang et al. (2010) method is used. This iterative approach implements binning and sub-binning of $\mathrm{LST_{norm}}$ values according to their corresponding fc values. The algorithm identifies the maximum value within each bin, and these maximum values collectively contribute to the determination of the dry edge. For a detailed understanding of these steps, it is recommended to refer to the study conducted by Tang et al. (2010). As to the wet edge, it is represented as a quasi-horizontal line relating the $T_{v,wet_{EB}}$ and $T_{s,wet_{EB}}$ simulated by the EB in the normalization step (under wet conditions, $T_{v,wet_{EB}}$ is marginally lower than $T_{s,wet_{EB}}$).

3.2.3 Sensitivity analysis to meteorological forcing and LST errors

A sensitivity analysis is undertaken to identify the input parameters whose deviation significantly changes the predicted output (Sanjeev et al., 2024). In this study, we assess the sensitivity of ET models' outputs to meteorological parameters (Ta, Rg, Ws, Rh) and LST uncertainties. The goal is to understand the differences in ET estimates of the TSEB_PT and LST_VI models using downscaled meteorological data

and observed/normalized LST in mountainous areas.

To conduct the sensitivity analysis, we incrementally adjust each input value by ±k%, one at a time, to determine the sensitivity order of the selected parameters. Time series simulations are run for each input variable using perturbed values. The overall sensitivity (S_p) of both models is calculated by summing the daily relative sensitivity (S_{pi}) values to changes in input parameter p over the entire time series (N days), as shown below (Zhan et al., 1996; Anderson et al., 1997; Sánchez et al., 2008):

$$S_p = \frac{1}{N}\sum_{Overpass\ dates} S_{pi} = \frac{1}{N}\sum_{Overpass\ dates}\left(\frac{LE(p_{altered+}) - LE(p_{altered-})}{LE_{baseline}}\right) \quad (10)$$

Where $LE_{baseline}$ is the LE estimate from high-resolution run, $LE(p_{altered\pm})$ is the LE estimate using the increased or decreased input value ($p_{altered+}$ *or* $p_{altered-}$) of one of the altered variables (Ta, Rg, Ws, Rh, and LST) with increments of ±k%. The percent change in LE estimates to ±k% change in an input is calculated using the relative error of $LE(p_{altered\pm})$ to $LE_{baseline}$ calculated as follow: $\frac{LE(p_{altered\pm}) - LE_{baseline}}{LE_{baseline}}$.

4. Results and discussion

In this section, the performance of both EB- and EF-based ET approaches over the mountainous study area is evaluated and intercompared. First, the quality of the meteorological forcing variables disaggregated and spatialized at the 30 m resolution is assessed against AWS measurements. Then, the 30 m resolution fluxes simulated by TSEB-PT are evaluated at the Tazaghart and Tahanaout EC sites. Next, an analysis of the topographic LST normalization procedure and of the performance of the LST-VI ET model is carried out, involving a comparison between simulated and Landsat LST over the study area and between the retrieved and observed fluxes at both EC sites respectively. Finally, the TSEB-PT and LST-VI ET modeling approaches are intercompared by focusing on the spatial variability of ET estimates within the study area.

4.1. Assessment of the 30 m resolution meteorological dataset

The scatterplots in Fig. 3 compare the spatially distributed (30 m) and the uncorrected (9 km) meteorological variables to AWS measurements at the Landsat overpass dates. Overall, the simulated 30 m resolution data show better agreement with ground measurements. The evaluation of the disaggregated Ta across six AWS locations shows an RMSE of 1.6 °C, an R-coefficient of 0.98 and almost no bias, indicating high accuracy. In contrast, the 9 km resolution ERA5-Land Ta data has an RMSE of 6.4 °C and an R of 0.79, and an overall bias of 3.3 °C (Fig. 3 (a)). This overestimation is particularly observed at the three elevated AWS locations (Neltner, Oukaimeden, and Tazaghart, all above 3200 m. a.s.l.), mainly due to the corresponding 9 km pixels average elevations being much lower than these sites elevations.

The evaluation of Rh for the 30 m resolution data shows an RMSE of 8.1 %, a bias of −4.2 %, and an R value of 0.73. This indicates moderate quality compared to Ta, but it is acceptable given Rh's lower impact on ET modeling relative to Ta and Rg. In contrast, the 9 km resolution ERA5-Land Rh data exhibit a higher RMSE of 12.1 %, a larger bias of 7.6 %, and a lower R value of 0.67, highlighting the accuracy improvement with higher resolution data (Fig. 3(b)). Despite showing less alignment with measurements than Ta due to the less accurate Tdew values used in calculating Rh, the high-resolution Rh data still demonstrate better correlation with measurements compared to the uncorrected low-resolution products.

The calibration of diffuse and reflected radiations obtained through the Samani-based approach against the DART model for modeling Rg shows a mean RMSE of 50 W/m^2 and an R value of 0.9. Although the DART model was tested and used for calibrating the Samani-based approach within a smaller area around the Aremd AWS and was not directly validated in this study, the simulated Rg values at a 30 m

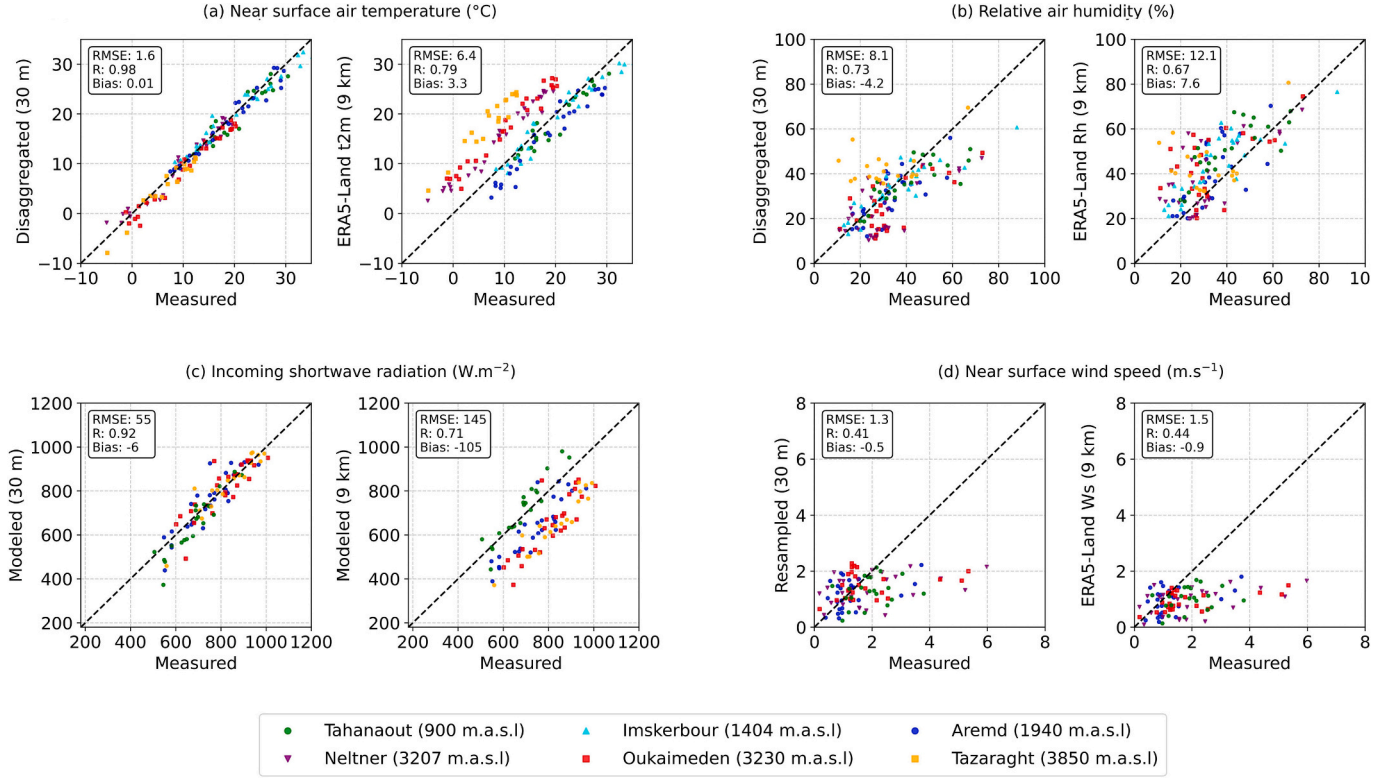

Fig. 3. Scatterplots comparing the 30 m and 9 Km meteorological products against ground measurements of Ta (a), Rh (b), Rg (c) and Ws (d) at the 6 AWS locations separately.

resolution compare well to ground measurements. The 30 m resolution data displays an RMSE of 55 W/m^2, a relatively insignificant bias of −6 W/m^2, and an R of 0.92, as depicted in Fig. 3(c). In contrast, the 9 km resolution ERA5-Land Rg data shows an RMSE of 145 W/m^2, a large negative bias of −105 W/m^2, and an R of 0.71, indicating a significant improvement with the 30 m resolution modeled data. This improvement is particularly evident in elevated areas. Pronounced underestimations of Rg are observed at Aremd, Oukaimeden, and Tazaghart, while the piedmont site Tahanaout shows reasonable alignment with measurements. Similar to Ta, this discrepancy is due to averaging values over the 9 km pixels. For elevated sites, the averages are lower compared to measurements, mainly due to the presence of shadowed pixels and slope orientations. In contrast, for the piedmont site, the average values closely match the site values due to gentle topography resulting in minimal variation in the 30 m pixel elevations and slopes within the 9 km area.

The left plot in Fig. 3(d) displays the 30 m resolution resampled ERA5-Land Ws compared to in-situ measurements. The RMSE, bias and R are estimated as 1.3 m/s, −0.5 m/s and 0.41, respectively. The results indicate a general agreement for low wind conditions (in-situ values below 2 m/s). However, as Ws increases, the disparity between the resampled ERA5-Land and measured values increases, with the underestimation becoming more pronounced. Despite the discrepancy observed, the 30 m resolution resampled ERA5-Land Ws is assumed applicable in our case, as the underestimation of Ws is only occasionally observed for strong wind. Comparatively, the 9 km derived ERA5-Land Ws data has an RMSE of 1.5 m/s, a bias of −0.9 m/s, and an R of 0.44. This slightly lower accuracy is expected, as the 9 km Ws data was only bilinearly resampled to 30 m.

4.2. Evaluation of TSEB-PT flux estimates

Table 3 reports the performance metrics of the TSEB-PT model when comparing the four simulated fluxes (Rn, G, LE and H) to in situ measurements at Tahanaout and Tazaghart EC sites. Due to the exclusion of snow and cloud periods and problems with tower-based flux measurements at the Tazaghart site, and cloudy scenes over the Tahanaout site, the modeled fluxes could be compared to measurements on 11 and 31 dates respectively. TSEB-PT estimates are assessed in two cases by using the 30 m resolution spatialized meteorological data (so-called Topo+ case) and the 9 km resolution ERA5-Land meteorological data (so-called Topo- case) as input to the ET model. Such a comparison allows for evaluating the impact of the spatial resolution of meteorological input data and their associated uncertainty to TSEB-PT flux estimates. The scatterplots of modeled versus measured fluxes for both cases are shown in Fig. 4.

At the Tazaghart site, the inclusion of topography leads to significant improvements in model performance, as shown by the drop in RMSE values for all flux components. In particular, Rn, LE, and H experience substantial reductions in RMSE, with values falling from 165 to 38 W/m^2 for Rn, from 100 to 50 W/m^2 for LE, and from 227 to 60 W/m^2 for H. The R values also indicate a better match between modeled and observed fluxes when topography is taken into account. Particularly, the R between simulated and observed H increases from 0.22 to 0.51. Furthermore, when using meteorological data at 30 m resolution as input to TSEB-PT, the bias between simulated and observed fluxes is much reduced, with values of −26, −18 and 2 W/m^2 for Rn, LE and H, respectively.

TSEB-PT is run with low-resolution meteorological inputs yields a tendency to underestimate Rn (bias of −161 W/m^2) despite the good correlation (R = 0.92). This underestimation seems to directly affect H (R = 0.22 and bias = −218 W/m^2) more than LE (R = 0.74 and bias = 84 W/m^2). This can be attributed to two key factors. Firstly, at low spatial resolution, the assumption of uniformity in mountainous regions results in a consistent underestimation of Rg mostly due to sub-grid shadowed slopes. Secondly, due to the elevated position of the site, the local Ta falls below the average value (an elevation difference of 1533 m). Regarding G, between the two runs (Topo +and Topo-), it exhibits a decreased bias of −15 W/m^2 and quite similar R and RMSE values, with R (RMSE) values of 0.78 (24 W/m^2) and 0.79 (30 W/m^{-2}) respectively.

On the relatively flat Tahanaout piedmont area, TSEB-PT simulated fluxes are less affected by topography. Nonetheless, significant improvements can still be observed by using 30 m resolution (instead of 9 km resolution) meteorological data as input. These improvements are visible for LE and H, as reflected by the increased R values by 0.24 and 0.11, as well as by the reduced RMSE values by 29 and 31 W/m^2 respectively. The absolute bias is also improved for both LE (from −19 to 9 W/m^2) and H (from 23 to −7 W/m2). Between the two runs, it can be observed that Rn experiences minimal variations, which is evident from the consistent metrics obtained. Comparatively, G also exhibits a level of stability, attributable to the intrinsic relationship between the two variables. Specifically, when high-resolution inputs are considered, the values of R, RMSE, and bias for Rn are found to be 0.93, 53 W/m^2, and 8 W/m^2 respectively, while for G, they are 0.60, 8 W/m^2, and 7 W/m^2 respectively.

Overall, compared to Tazaghart, the absence of complex topography and substantial elevation gradients in Tahanaout surroundings results in less significant changes between Topo+ and Topo- cases. The relative difference of elevation between the site and corresponding ERA5-Land pixel elevations is approximately 11 % with a standard deviation of 80 m within the 9 km pixel. It turns out that averaged Rg and ERA5-Land Ta at 9 km spatial resolution closely match the local measurements at this foothill site, which explains the smaller differences in ET estimates between the two runs.

4.3. Evaluation of EF-based flux estimates

4.3.1. Assessment of LST topographic normalization

Normalizing LST for topographic effects is a prerequisite for applying the EF-based ET model. Since the normalization procedure is based on an EB to simulate LST in a range of meteorological conditions (in particular a range of Rg and Ta values), a first assessment of the LST

Table 3
Performance metrics of TSEB-PT flux estimates at the Tazaghart and Tahanaout EC sites for input meteorological data at 30 m (Topo+), and at 9 km (Topo-) resolution (shown in parentheses).

		Rn	G	LE	H
Tazaghart site[a]	RMSE(W/m^2)	38 (165)	23 (41)	50 (100)	60 (227)
	Bias (W/m^2)	−26 (−161)	−10 (−26)	−18 (84)	2 (−218)
	R (−)	0.95 (0.92)	0.78 (0.76)	0.63 (0.74)	0.51 (0.22)
Tahanaout site[b]	RMSE(W/m^2)	53 (55)	8 (8)	70 (99)	44 (75)
	Bias (W/m^2)	8 (10)	7 (7)	9 (−19)	−7 (23)
	R (−)	0.93 (0.92)	0.6 (0.64)	0.81 (0.57)	0.78 (0.67)

[a] EC Tazaghart was installed in September 2020, with two major shutdowns due to high winds in the springs of 2021 and 2022. Local validation dates correspond to snow and cloud-free periods in the summers of 2021 (4 dates) and 2022 (7 dates).

[b] EC Tahanaout was dismantled in May 2022. All cloud-free dates from September 2020 to April 2022 were used for validation: 5 dates in 2020, 16 dates in 2021, and 9 dates in 2022. More details can be found in Fig. 6.

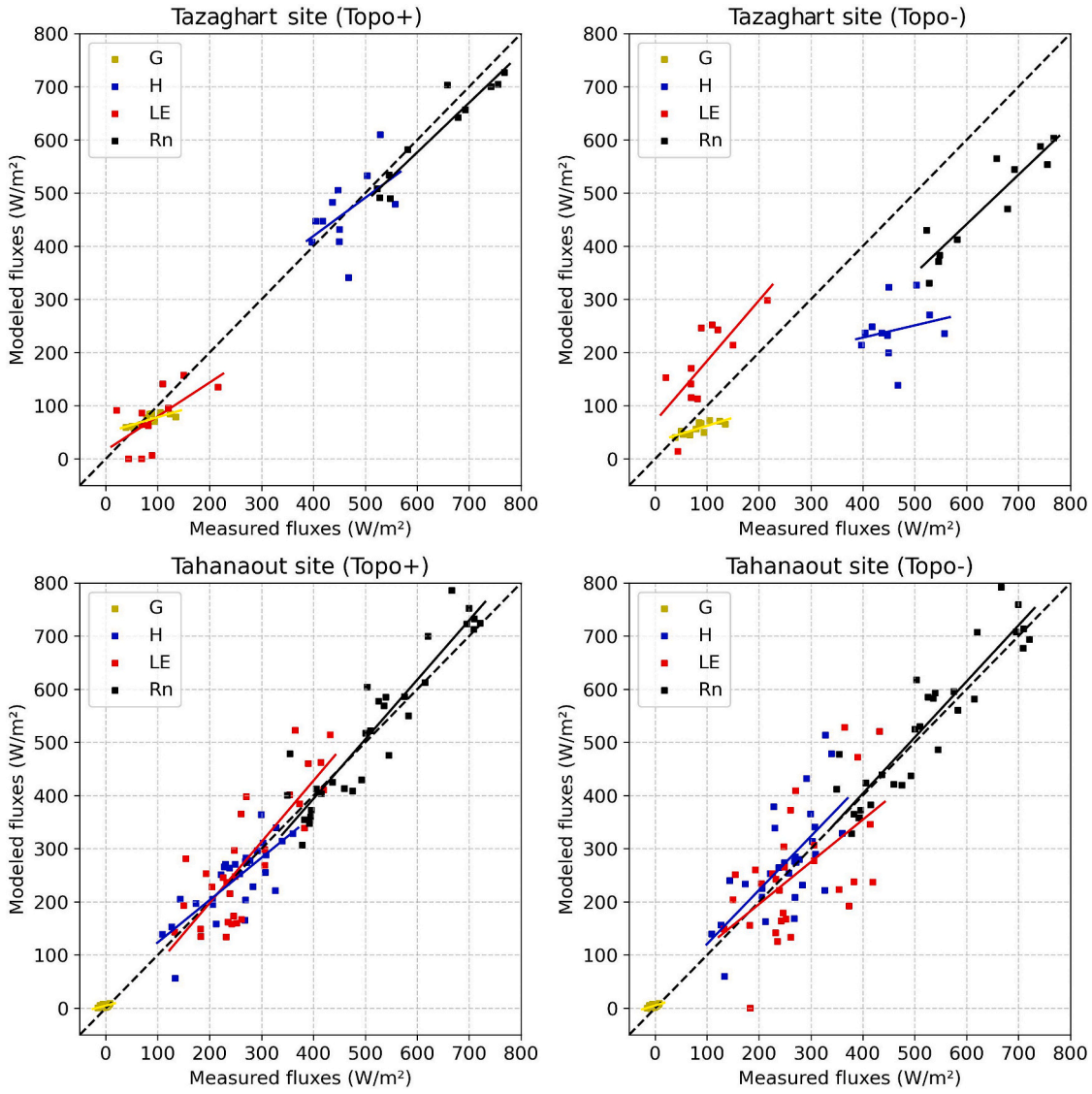

Fig. 4. Scatterplots of TSEB-PT simulated fluxes versus in situ measurements at Tazaghart (top row) and Tahanaout (bottom row) EC sites for the Topo+ (left column, using 30 m resolution meteorological data as input) and Topo- (right column, using 9 km resolution meteorological data as input) cases separately. Regression lines match the colors of their corresponding fluxes.

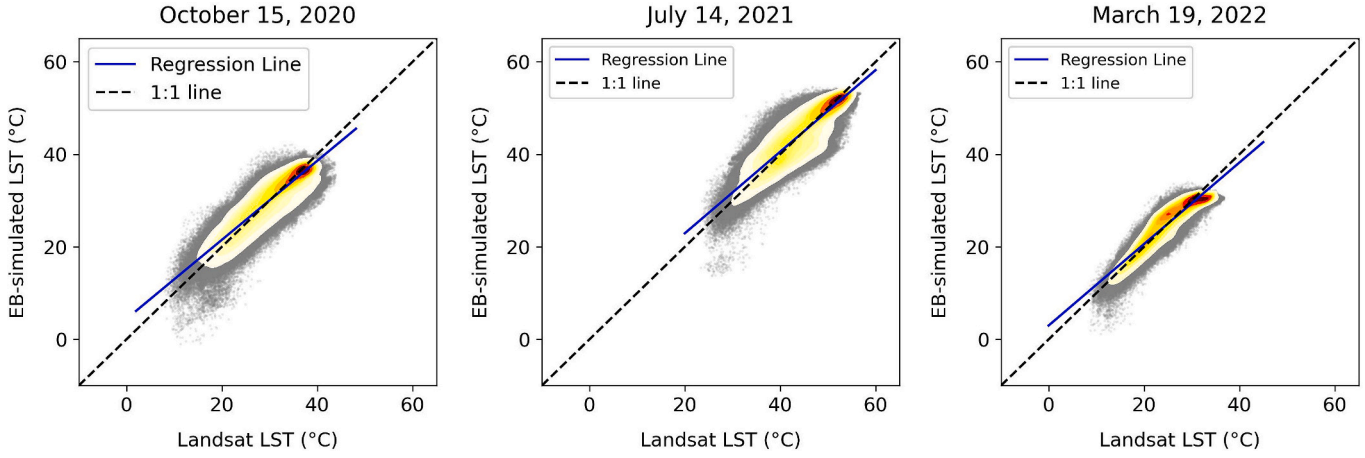

Fig. 5. Scatterplots of EB-simulated versus Landsat LST over the study area for three selected dates separately. Red colour indicates higher density of points, and white colour lower density. (For interpretation of the references to colour in this figure legend, the reader is referred to the web version of this article.)

normalization step is proposed by comparing the EB-simulated to the Landsat LST.

Fig. 5 shows scatterplots of simulated versus Landsat LST for three dates selected for their contrasted conditions: July 14, 2021 (hot dry date in summer), March 19, 2022 (wet date in growing season) and October 15, 2020 (intermediate date). The scatterplots show satisfying results, and the consistency between the three selected dates reflects a certain robustness of the EB inversion technique. The EB-based inversion model reproduced the spatial patterns of the observed Landsat LST with an R greater than 0.9 for these three dates, and RMSE values of 2.7 °C, 2.8 °C and 2.0 °C for the intermediate, dry, and wet dates, respectively. The chart of Fig. 6 details the obtained R and RMSE values between the EB-based inverted and Landsat LST for all Landsat overpass dates separately. Note that a considerable number of pixels were contaminated by clouds and cloud shadows on several October dates from 2020 to 2022. This could explain why the results are slightly poorer in October for each year than during the remaining period. The mean R and RMSE for all dates are 0.89 and 2.8 °C, respectively. Note that all biases are canceled out as a result of the calibration procedure of the normalization model using Landsat LST observations (i.e., the minimization of the RMSE during the inversion of f_{ss} and f_{sv} parameters).

The effectiveness of the normalization procedure in reducing topographic effects on LST data is illustrated in Fig. 7. When looking at the LST images before and after normalization in Fig. 7, one observes that the elevated parts of the study area show a significant increase in LST with the topographic correction. Additionally, a significant contrast in LST still remains after normalization. These variations can be attributed to the diversity of vegetation and soil moisture conditions in the riparian zones along the Rheraya river, the agricultural zones located downstream, and the cedar forest that crosses from east to west.

Examination of the LST-VI feature space after topographic normalization, as illustrated by the scatterplots in Fig. 7, reveals a distribution that closely reflects typical patterns observed in flat regions (Stefan et al., 2015). Notably, the topographic normalization method considerably reduced the presence of pixels located outside the LST-VI (prior to topographic normalization) polygon constructed using the four EB-simulated temperature endmembers ($T_{s,\ dry}$; $T_{v,\ dry}$; $T_{s,\ wet}$; and $T_{v,\ wet}$), specifically those above or below the boundaries defined by the dry and wet edges estimated by the EB model. This result is particularly noteworthy for pixels close to the wet edge, where distortions caused by low values of fc and LST can occur, as shown in the scatters presented in Fig. 7.

Before applying the contextual formula (eq. 3) to estimate EF for any point in the LST-VI feature space, the determination of the dry edge is further consolidated by using Tang et al. (2010) approach. For illustration, Fig. 8 plots the normalized LST-VI feature spaces overlaid with the dry edge simulated by the EB model and estimated by Tang et al. (2010) technique. An interesting feature is that simulated and observed dry edges are quasi parallel for the three dates (and overlap in the scatterplot on the right), which is an indicator of the consistency between the two approaches.

4.3.2. Evaluation of LST-VI flux estimates

The performance metrics of the LST-VI ET model are shown in Table 4. The four simulated fluxes (Rn, G, LE, and H) are compared to in-situ measurements at Tahanaout and Tazaghart EC sites. The comparison is conducted for three input cases: 1) using topographically normalized LST_{norm} and high-resolution (30 m) meteorological data (Topo+ case), 2) using Landsat LST and high-resolution (30 m) data (intermediate case), and 3) using Landsat LST and low-resolution (9 km) data (topo- case). Such a comparison allows for evaluating the impact of the normalization procedure and high-resolution meteorological forcing on LST data to LST-VI flux estimates. The scatterplots of modeled versus measured fluxes for the three cases are shown in Fig. 9.

The Tazaghart site is a convincing example of the effectiveness of LST topographic normalization. When the traditional LST-VI model is applied directly, as is generally the case over flat regions, it leads to an overestimation of LE even when using high-resolution meteorological data as input. This overestimation can be attributed to the unique characteristics of the location of this very high site, where LST tends to be colder, and therefore, when not normalized it stands further from the dry edge. Consequently, the increased distance from the dry edge leads to higher EF values, ultimately resulting in an overestimation of LE (as evidenced by a bias of 100 W/m^2), and an underestimation of H (bias of −116 W/m^2). Before normalization, both the simulated LE and H show large RMSE values for the Intermediate case (109 and 125 W/m^2, respectively). After normalization, results are much improved for LE (and H) with an RMSE of 45 W/m^2 (54 W/m^2), a bias of 13 W/m^2 (−24 W/m^2), and an increase in R (by 0.16) in case of H.

As the same Rn (and G) values were used for LE and H estimation in both Topo+ and Intermediate cases (high-resolution meteorological forcing), their metrics remain consistent with an RMSE of 38 W/m^2 (−23 W/m^2), an R of 0.95 (0.78) and a bias of −25 W/m^2 (−12 W/m^2), respectively. As to the Topo- run, a large bias is introduced in Rn (−161 W/m^2) which seems to affect H (−193 W/m^2) and brings down LE's bias from 100 W/m^2 to 58 W/m^2 in comparison to intermediate run. RMSE and R values are 165 W/m^2 and 0.92 for Rn, 73 W/m^2 and 0.77 for LE, and 197 W/m^2 and 0.66 for H. The metrics for G are slightly degraded (RMSE = 41 W/m^2, bias = −26 W/m^2, and R = 0.76) which is attributed to the relatively smaller magnitude of G when compared with other

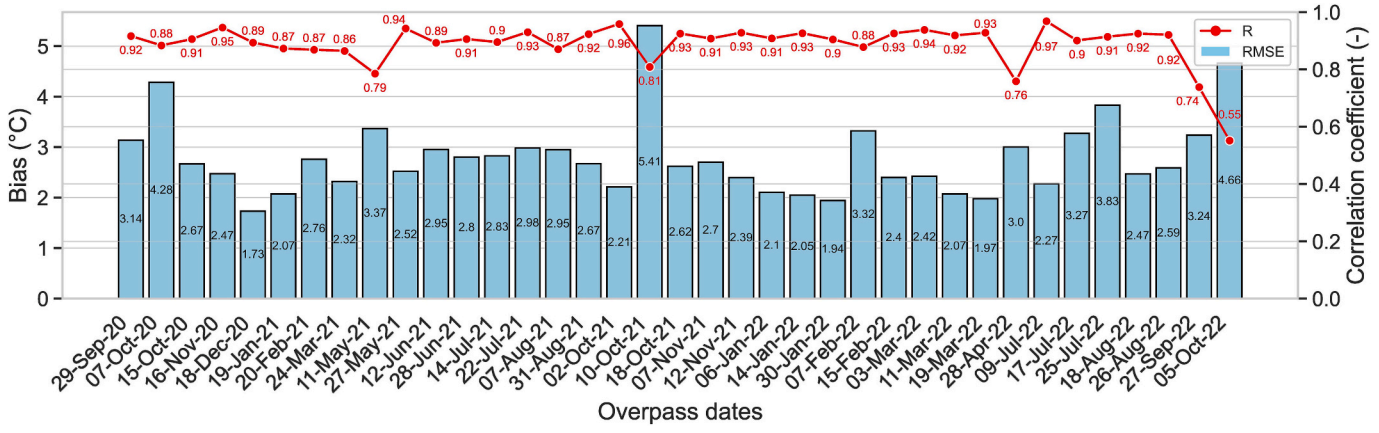

Fig. 6. RMSE and R between simulated and Landsat LST over the study area for each Landsat overpass date separately. Numerical values of RMSE and R are shown inside bars in black colour, and next to scatter points in red colour, respectively. (For interpretation of the references to colour in this figure legend, the reader is referred to the web version of this article.)

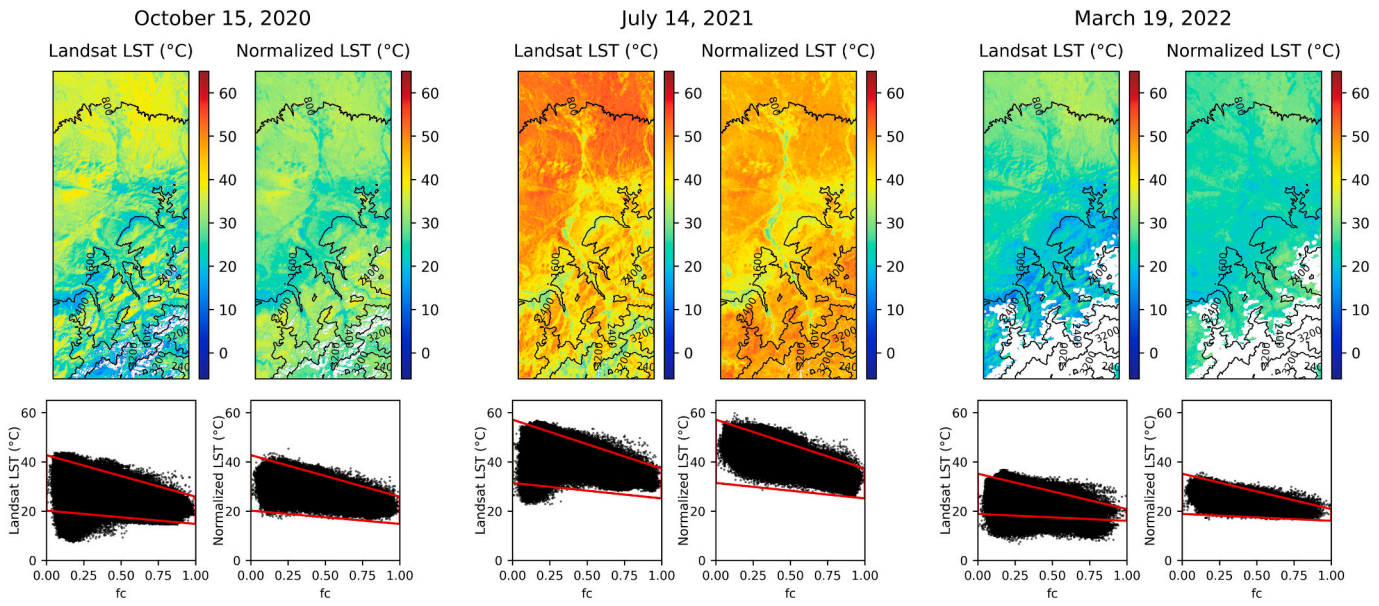

Fig. 7. LST maps (top) and LST-VI feature spaces (bottom) before (left) and after (right) normalization for topographic effects on three Landsat overpass dates separately. Black lines represent the elevation contour. Red quadrilaterals vertices represent the temperature endmembers ($T_{v,dry_{EB}}$, $T_{v,wet_{EB}}$, $T_{s,dry_{EB}}$, and $T_{s,wet_{EB}}$) simulated by the EB model. (For interpretation of the references to colour in this figure legend, the reader is referred to the web version of this article.)

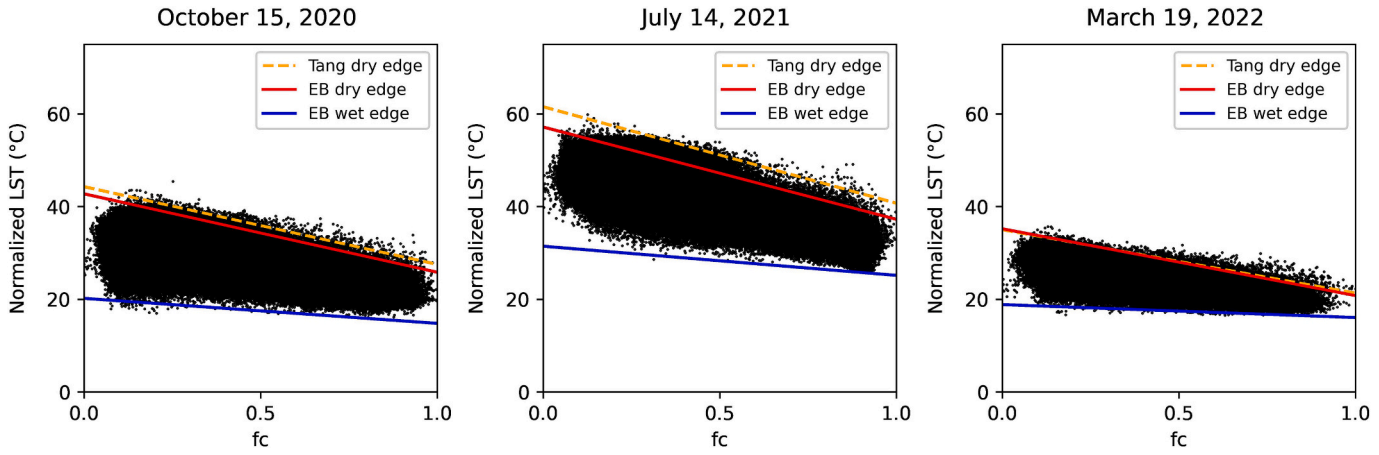

Fig. 8. Normalized LST-VI feature spaces overlaid with the wet edge simulated by the EB model (blue line), the dry edge simulated by the EB model (red line) and the dry edge determined by Tang et al. (2010) method (orange dotted line). (For interpretation of the references to colour in this figure legend, the reader is referred to the web version of this article.)

fluxes.

The improved performance of the LST-VI ET model after LST normalization is also illustrated at the Tahanaout site although to a much lesser extent. The bias values between simulated and measured LE and H are −3 and 1 W/m^2, respectively, which are slightly better than the values of −10 and 8 W/m^2 for the Intermediate case and − 31 W/m^2 and − 12 W/m^2 when switching to Topo- configuration. Similarly, the RMSE values are slightly reduced for LE going from 62 to 56 and then to 52 W/m^2, and for H, dropping from 50 to 49 and finally to 48 W/m^2 across the three runs (Topo-, Intermediate, and Topo+). Additionally, switching from Topo+ to Topo- runs, no significant changes are observed in R values for LE (0.77 against 0.78 and 0.77) and H (0.81 against 0.79 and 0.77).

For Topo+ and Intermediate cases, the metrics for Rn (RMSE = 53 W/m^2, R = 0.93, and bias = 28 W/m^2) and G (RMSE = 30 W/m^2, R = 0.56, and bias = 30 W/m^2) showed good and moderate match to measurements, respectively. The use of low-resolution meteorological inputs (Topo-) resulted in no significant changes. The only noticeable change was a slight underestimation in Rn, which shifted from a bias value of 28 to −15 W/m^2. As was clarified earlier, the gentle slopes and the negligible elevation difference between the foothill site's location and corresponding ERA5-land's pixel explains the small differences in Rn (and eventually G) estimates for all runs.

In contrast to the Tazaghart site, overall, the model run with non-normalized LST data at the Tahanaout site results in no significant change. This is attributed to the same reason as that highlighted when using the TSEB-PT model and can be analyzed from two points of view: 1) whether LST underwent normalization process or it was used in its original form, and 2) the fineness of resolution (high or low) of the meteorological forcing data. On one hand, the LST normalization for the meteorological effects induced by topography brings minimal changes to LST at Tahanaout being a foothill site. Additionally, given the triangular shape of the feature space formed by the wet and dry edge, which narrows at higher fc values, one would anticipate closely aligned EF values when using normalized and original Landsat LST. On another hand, the slight slopes and minimal difference between foothill site and

Table 4
Performance metrics of LST-VI model at the Tazaghart and Tahanaout EC sites for Topo+ run (LST_{norm} and input meteorological data at 30 m), intermediate run (Landsat LST and input meteorological data at 30 m), and Topo- run (Landsat LST and input meteorological data at 9 km). Table values are represented as: Topo+ (intermediate, Topo-).

		Rn	G	LE	H
Tazaghart Site[a]	RMSE(W/m^2)	38 (38, 165)	23 (23, 41)	45 (109, 73)	54 (125, 197)
	Bias (W/m^2)	−25 (−25, −161)	−10 (−10, −26)	13 (100, 58)	−24 (−116, −193)
	R (−)	0.95 (0.95, 0.92)	0.78 (0.78, 0.76)	0.60 (0.62, 0.63)	0.65 (0.49, 0.59)
Tahanaout site[a]	RMSE(W/m^2)	53 (53, 52)	30 (30, 29)	52 (56, 62)	48 (49, 50)
	Bias (W/m^2)	28 (28, −15)	30 (30, 28)	−3 (−10,−31)	1 (8, −12)
	R (−)	0.93 (0.93, 0.92)	0.56 (0.56, 0.57)	0.77 (0.78, 0.77)	0.81 (0.79, 0.66)

[a] the validation dates align with those detailed in Table 3.

corresponding ERA5-land's pixel elevations explain the minor differences in Rn (and consequently G) estimates between high- and low-resolution runs.

4.4. Discussions

4.4.1. Quantitative comparison between EB- and EF-based ET models

At the Tazaghart site, the surface energy, used for determining H and LE, is similarly calculated using both EF- and EB-based models. This consistency arises due to the site's pixel being processed as a single-source surface in the EB-based model. Hence, neither surface anisotropy nor bidirectional effects are considered during the retrieval of both longwave and shortwave net radiation. For the Topo+ run, the resulting metrics are: RMSE = 38 W/m^2, bias = −25 W/m^2, and R = 0.95. For Topo-, the values are: RMSE = 165 W/m^2, bias = −161 W/m^2, and R = 0.92.

However, at the vegetated Tahanaout site, the TSEB-PT model considers those effects and demonstrates a slightly lower absolute bias in Rn than the LST-VI model (8 W/m^2 against 28 W/m^2 for Topo+ and 10 W/m^2 against −15 W/m^2 for Topo-). Despite this minor discrepancy, Rn and G, whether used in the LST-VI approach or computed using the TSEB-PT model, produce quite similar metrics across all runs at both sites. The localized comparison in the following focuses on LE and H fluxes.

Accounting for the influence of topography (the Topo+ case), TSEB-PT model has an RMSE of 50 W/m^2, a bias of −18 W/m^2, and an R of 0.63. In contrast, the LST-VI model shows a reduced RMSE (45 W/m^2) and a lower absolute bias (13 W/m^2), while a marginally lower correlation (0.60). For the H flux at the same site, the TSEB-PT model shows an RMSE of 60 W/m^2, a bias of 2 W/m^2, and an R of 0.51. The LST-VI

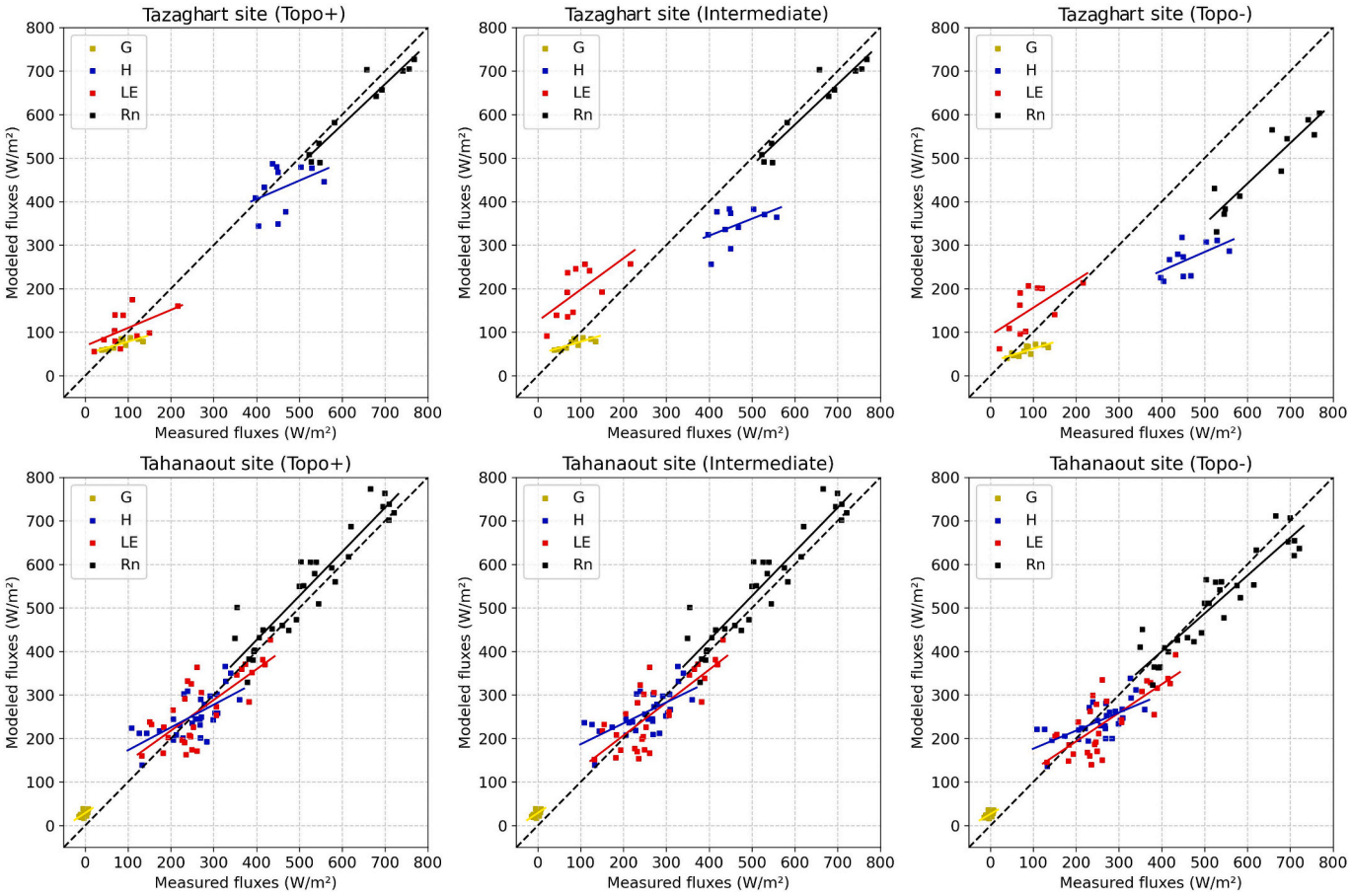

Fig. 9. Scatterplots of LST-VI simulated fluxes versus in situ measurements at Tazaghart (top row) and Tahanaout (bottom row) EC sites for the Topo+ (left column, using the normalized LST_{norm} data and high-resolution meteorological data as input), Intermediate (middle, using the original LST data and high-resolution meteorological data as input) and Topo- (right column, using the original LST data and low-resolution meteorological data as input) cases separately.

model performs slightly better in terms of RMSE (54 W/m^2) and R (0.65) but shows a larger negative bias (−24 W/m^2). At the Tahanaout site, the TSEB-PT model for the LE flux has an RMSE of 70 W/m^2, a bias of 9 W/m^2, and an R of 0.81. In contrast, the LST-VI model again exhibits a lower RMSE (52 W/m^2) and a lower bias (−3 W/m^2), but with a slightly lower correlation (0.77). For the H flux, the TSEB-PT model reports an RMSE of 44 W/m^2, a bias of −7 W/m^2, and an R of 0.78. Comparatively, the LST-VI model shows a slight increase in RMSE (48 W/m^2), a positive bias (1 W/m^2), and a slight improvement in R (0.81).

When examining the metrics for the Topo- case, the comparison between the TSEB-PT and LST-VI models offers some key insights on their sensitivity. At the elevated Tazaghart site, the TSEB-PT estimated LE flux shows an RMSE of 100 W/m^2 and a bias of 84 W/m^2, with an R of 0.75. In contrast, the LST-VI model yields better accuracy, with a lower RMSE of 73 W/m^2 and a smaller bias of 58 W/m^2, albeit a lower R value of 0.63. As for the H flux at the Tazaghart site, the TSEB-PT model's RMSE and bias, at 227 W/m^2 and − 218 W/m^2 respectively, are larger in absolute value than the LST-VI model's corresponding values of 197 W/m^2 (RMSE) and − 193 W/m^2 (bias). Moreover, the LST-VI model exhibits a stronger correlation between predicted and observed values, with an R value of 0.59 versus the TSEB-PT model's R value of 0.22.

Switching to the foothill site of Tahanaout, when evaluating the LE flux, the TSEB-PT model in comparison to the LST-VI approach, exhibits a larger RMSE (99 against 62 W/m^2) and a lower correlation (0.57 against 0.77). Although the TSEB-PT model shows a smaller bias (−19 W/m^2 versus −31 W/m^2), suggesting less underestimation, the LST-VI model's lower RMSE and R value closer to 1 suggest a better overall predictive performance for LE flux at this site. When assessing H flux at the Tahanaout site, the TSEB-PT model provides reasonable results with an RMSE of 75 W/m^2, an R value of 0.67, and a bias of 23 W/m^2. However, the LST-VI model delivers slightly better performance metrics, with an RMSE of 50 W/m^2, an R value of 0.77, and a bias of −12 W/m^2.

In essence, following the above evaluation of TSEB-PT and LST-VI, both models demonstrate closely matched performance metrics across the two distinct EC sites when considering the influence of topography. Notwithstanding the similarities, the LST-VI model generally shows slight improvements in terms of RMSE and absolute bias values for both sites and both turbulent fluxes. However, the R values are mixed, in some cases, the TSEB-PT model shows better R values, indicating a better fit to the observed data. Furthermore, when focusing on the Topo- case, the LST-VI model also tends to outperform the TSEB-PT, providing less deviated predictions for both LE and H fluxes across both EC sites, as evidenced by their comparative metrics. The overall slightly superior performance of the LST-VI model can be credited to the process of topographic normalization of LST, coupled with its relatively simpler requirements for input variables and parameters. Compared to the TSEB-PT model, this simplicity makes the LST-VI model less susceptible to uncertainties that are tied to these inputs.

4.4.2. *Assessment of the spatial distributions of LE and EF estimates*

The spatial differences and similarities in the LE and EF simulated by both models are qualitatively examined over the entire study area. Fig. 10 presents for the three dates selected for their contrasted overall conditions (wet on 10/15/2020, dry on 07/14/2021 and intermediate on 03/19/2022) the maps of instantaneous LE estimated by taking into account topography (Topo+ case) using TSEB-PT and LST-VI models separately. The maps of NDVI and Rg on those dates are also shown for analyses purposes.

At the scale of the study area, the spatial distribution of LE looks relatively similar for both models. The apparent alignment is particularly true on wet and intermediate dates, but it is less prominent on the dry date. At a finer scale upon closer inspection, there are disparities between the results of the models even on wet and intermediate dates. These differences are most apparent in steeply sloping areas, where there is a clear contrast in slope on either side of the ridges found in the higher parts of the area. The divergence in results between the two models probably stems from their unique approaches to managing and correcting terrain topography.

For a more quantitative analysis, the scatterplots between TSEB-PT and LST-VI simulated LE are showcased in Fig. 11 over the entire study area (roughly 1 million pixels) for the three selected dates separately. The clustering of data points, along with the resulting metrics, further confirms the observations discerned from the maps. High correlation (0.88 and 0.85), and a low mean difference (−14 and 17 W/m^2) between the LE simulated by both models are obtained for the wet and intermediate dates respectively. The same metrics are degraded for the dry date with a correlation and mean difference of 0.74 and 70 W/m^2, respectively.

Two hypotheses could explain the larger difference between TSEB-PT and LST-VI LE estimates on the dry date. On one hand, it is well known that uniformly low soil moisture makes it particularly difficult to identify the actual wet edge. Although our study area is large enough to encompass a wide range of pixels with varying soil moisture and fractional vegetation cover, the contextual ET approach is potentially biased under drought conditions (Long and Singh, 2012; Long et al., 2012; de Tomás et al., 2014; Chen and Liu, 2020).

On the other hand, when using EB-based ET models in drought conditions, considerations need to be made regarding the level of water stress by adjusting the excess aerodynamic resistance to heat transfer relative to momentum transfer (kB^{-1} parameter). Research, such as that by Gokmen et al. (2012), underscores a progressive reduction in kB^{-1} as water stress levels intensify. However, in our approach, we did not adjust kB^{-1} values based on intensifying water stress levels. Instead, we set average values that provided the most favorable outcomes, such as a value of 2 for the bare soil class. This decision is further complicated by the fact that literature presents a lack of consensus regarding the optimal values for this coefficient, with a diverse range of values being reported (e.g., Kustas et al., 1989; Troufleau et al., 1997; Verhoef et al., 1997; and Yang et al., 2008).

To further assess the spatial distribution of the LE simulated by TSEB-PT and LST-VI approaches, an additional analysis is carried out by examining the contrast between east- and west-facing slopes. The rationale for focusing on the east-west gradient, as opposed to the north-south for instance, lies in the assumption that soil moisture (and therefore EF) can be considered relatively uniform. If the correction for topography in TSEB-PT and LST-VI ET approaches was efficient, then the distribution of the EF simulated in east- and west-facing slopes should be rather similar. Note that over the course of a day, the amount of radiation received on the east and west slopes is nearly identical. But at the time (around 11 am) of Landsat overpass, Rg is expected to be larger on east- than on west-facing slopes. Consequently, at constant EF, the simulated LE should be larger in east- than in west-facing slopes. This is why the east-west gradient of EF (instead of the east-west gradient of LE) is used here as an indicator of the performance of ET modeling approaches in the mountains.

The aspect of the terrain makes it possible to extract and separate the pixels (and their associated Rg, LE, EF values) in east- and west-facing slopes. By setting an altitude threshold at 1600 m.a.s.l., it becomes possible to pinpoint areas that not only manifest distinct directional characteristics but also present marked steepness.

Fig. 12 showcases the spatial distribution of Rg and of the EF and LE simulated by TSEB-PT and LST-VI separately. The observed disparity of Rg distributions in the east- and west-facing slopes is in line with expectations. Given that the satellite overpass occurs at around 11 am, the land to the east naturally receives more energy with an average difference of 487 W/m^2.

When looking at EF distributions in Fig. 12, the TSEB-PT model provides asymmetrical distributions in east- and west-facing slopes. The dominant value across all dates for land to the west is zero. This is especially noticeable on the dry date, when zero LE is reached by 60 % of the pixels. In contrast, the LST-VI model appears to perform more uniformly as the EF distributions in east- and west-facing slopes are very

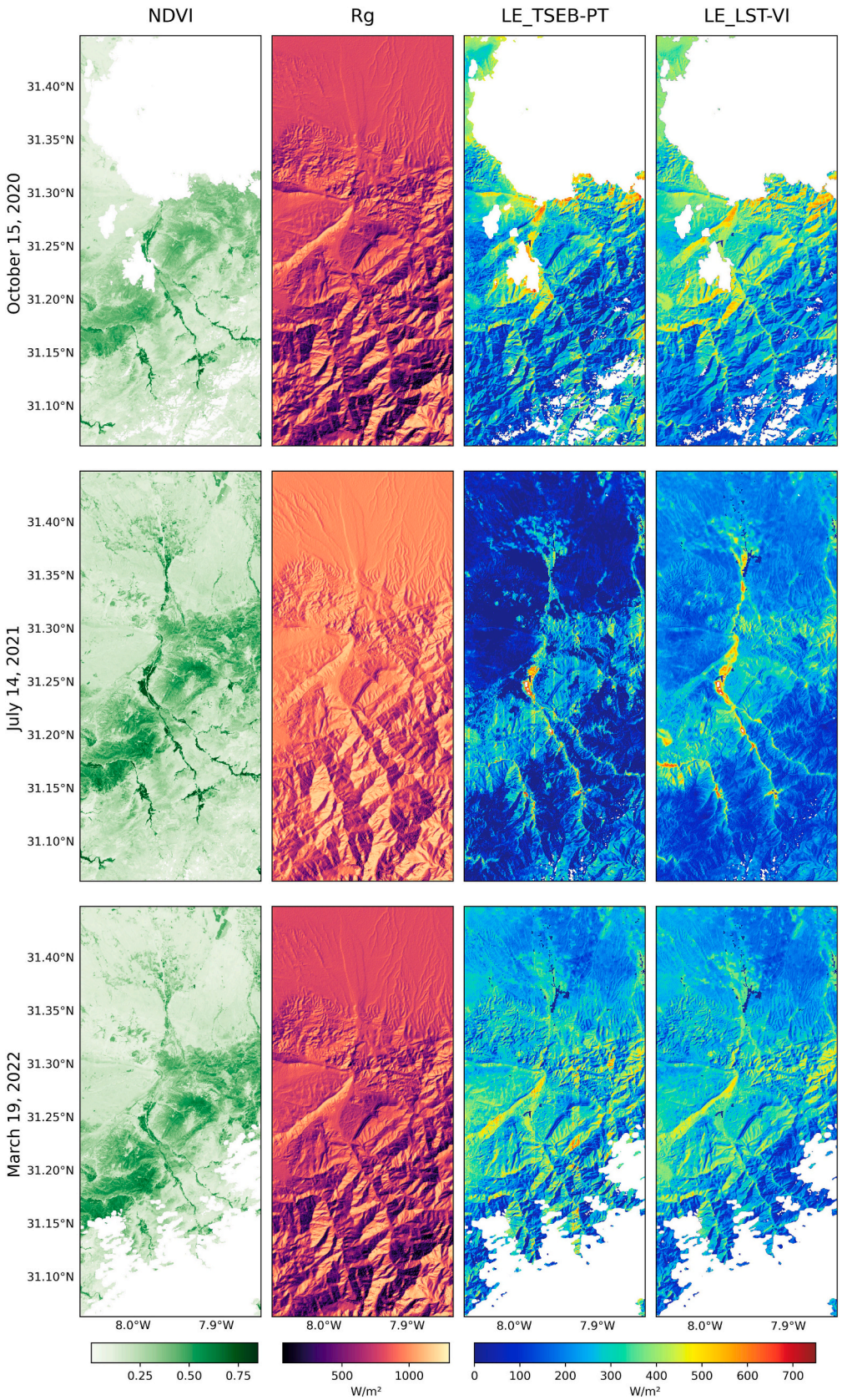

Fig. 10. Maps of NDVI (Left column), modeled Rg (central left column), and modeled LE simulated by TSEB-PT (central right column) and LST-VI models (right column) are shown for each of the three selected dates (rows 1–3).

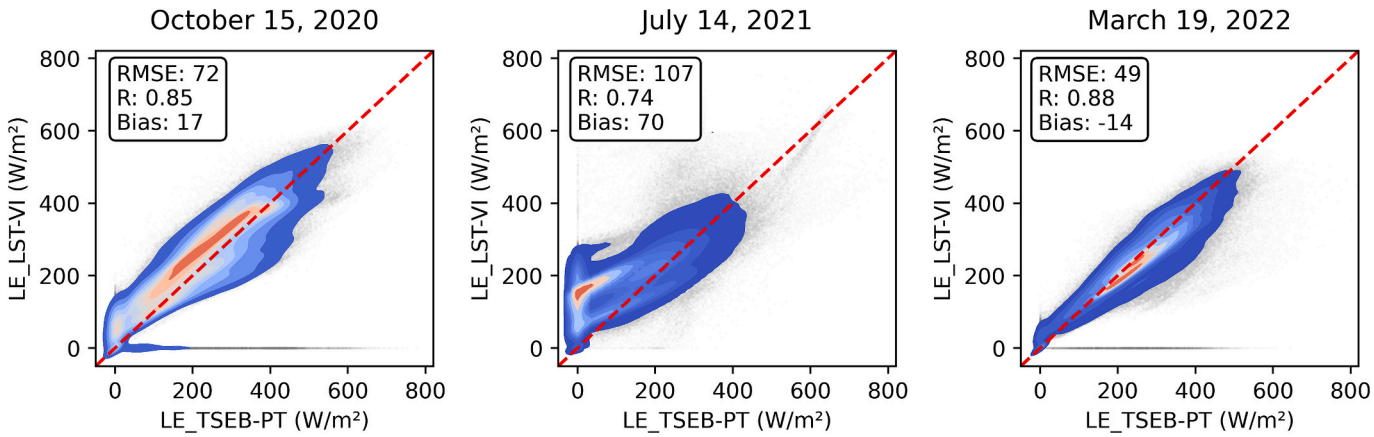

Fig. 11. Density scatterplots of LST-VI versus TSEB-PT modeled LE for the three selected dates separately. The red. (For interpretation of the references to colour in this figure legend, the reader is referred to the web version of this article.)
dashed line represents the (1,1) line. The colour gradient represents the density of points, where a shift towards red means a higher point density, while a transition towards blue indicates a lower point density.

consistent. Although no spatially distributed soil moisture (or flux) measurements were available to assess the actual variability of EF in east- and west-facing slopes, the results indicate that the LST-VI ET modeling approach effectively corrects for topographic effects regardless of Rg. Supporting this analysis with quantitative metrics, the EF contrast for east versus west is consistent at an absolute value of 0.01 across all dates for the contextual method. Comparatively, the EF contrast for TSEB-PT varied with wetness/dryness conditions: 0.20, 0.14 and 0.23 for wet, dry, and intermediate conditions, respectively (average contrast of 0.19).

When looking at the LE distributions in Fig. 12, the LE contrast between east and west for TSEB-PT model is 205, 107, and 173 W/m^2, for the wet, dry, and intermediate date respectively. Comparatively, the LST-VI model reports LE contrasts of 156, 79, and 153 W/m^2 for the same dates respectively. Differences in LE estimates between east- and west-facing slopes are more difficult to interpret than differences in EF estimates, because LE depends on both Rg and EF. However, the lower east-west LE gradient observed for LST-VI than for TSEB-PT model is due to the lower EF gradient observed for LST-VI model.

4.4.3. Sensitivity analysis results

In sensitivity analysis, a typical input variation range of ±10 % (k = 10) is often assumed. However, this assumption may not accurately reflect the uncertainty for certain inputs and could be overly conservative for others, especially in mountainous regions where topography significantly influences the spatial distribution of these inputs. To account for the pronounced effects of elevation and sun exposure, the variations in LST and Ta are adjusted up to ±15 % (in degrees Celsius), corresponding to potential ranges of ±0.5 °C to ±6.3 °C for LST and ± 1.7 °C to ±5.1 °C for Ta at fluxes stations. For Rg, the commonly assumed ±5 % variation (e.g., Sánchez et al., 2008) is unrealistic for mountainous areas. Consequently, Rg is varied by up to ±25 %, corresponding to ranges of ±21 W/m^2 to ±243 W/m^2. The same adjustment percentage is applied to perturb Ws and Rh, with potential variations of ±0.05 m/s to ±2 m/s for Ws and ± 2.5 % to ±17.5 % for Rh.

A list of the input variables, as well as their assigned uncertainties and resulting S_p by site, are provided in Table 5. Average S_p values greater than 20 % are denoted in bold to indicate parameters that have a significant effect on LE retrieval. Accompanying Table 5, tornado charts that visually depict the percent change in simulated LE in response to a ± k% change in each input variable are featured in Fig. 13.

Interestingly, Ws shows a small influence on LE at Tahanaout, but its effect becomes more significant at Tazaghart, likely due to stronger winds at higher altitudes. Changes in Ws up to ±25 % result in LE changes of up to 34 % at Tazaghart, making it more influential than Ta at this site. In contrast, Rh remains insignificant at both sites, showing minimal sensitivity values and negligible changes in LE.

In contrast, for the LST_VI model, Rg emerges as the most critical input affecting LE at both sites, (although to a lesser extent compared to TSEB_PT), indicating that solar exposure significantly impacts LE estimates in the LST_VI model. At Tahanaout, Sp values for Rg reach 0.68 at ±25 %, resulting in LE changes of up to 36 %. At Tazaghart, the sensitivity to Rg is higher, with an Sp value of 0.91 at ±25 %, leading to LE changes of up to 49 %. Only larger perturbations (greater than ±12.5 %) in LST and Ta begin to affect LE significantly. Ws and Rh have minimal impact on LE estimates at both sites, and Rh shows negligible effects. To avoid confusion, please note that the LST-VI does not require Ws or Rh as direct inputs. Instead, these variables are indirectly used in the LST normalization process, which then serves as input for the contextual model.

The overall reduced sensitivity observed in the LST_VI model can be attributed to three main factors: 1) the contextual approach is known for requiring fewer inputs compared to physically based models, 2) estimations of EF and Rn are independent from each other by this method, and 3) the reduced sensitivity of the LST normalization process. In fact, although LST normalization utilizes a dual-source energy balance LST inversion and relies on the same meteorological forcing as TSEB_PT, Newton's iterative process significantly reduces errors between the inverted LST and observed Landsat LST. This effectively minimizes the impact of uncertainties in the inputs on LST normalization, thereby reducing errors in EF retrieval. Conclusively, the sensitivity of the LST_VI model is primarily related to perturbations in Rn components, which are functions of Rg, Ta, and LST, with Rg being the dominant factor under clear-sky conditions in a semi-arid climate.

Finally, it has been demonstrated that Rg, LST, and, to a lesser extent, Ws significantly impact LE retrieval using the TSEB_PT model at higher elevations. The LST_VI model, which is also sensitive to Rg but corrects for topographic effects and uses normalized LST instead of observed Landsat LST, maintains uniform EF estimates. This suggests that the variability in EF between east- and west-facing slopes observed in the TSEB_PT model is primarily due to its sensitivity to LST variations and secondarily to Ws. Notably, as mentioned earlier, Ws is not a direct input to the LST_VI model and is the only meteorological variable that was resampled in this study.

4.4.4. Additional remarks on spatialization capabilities of EB- and EF-based modeling approaches in mountains

TSEB-PT is known for being highly sensitive to the considerable

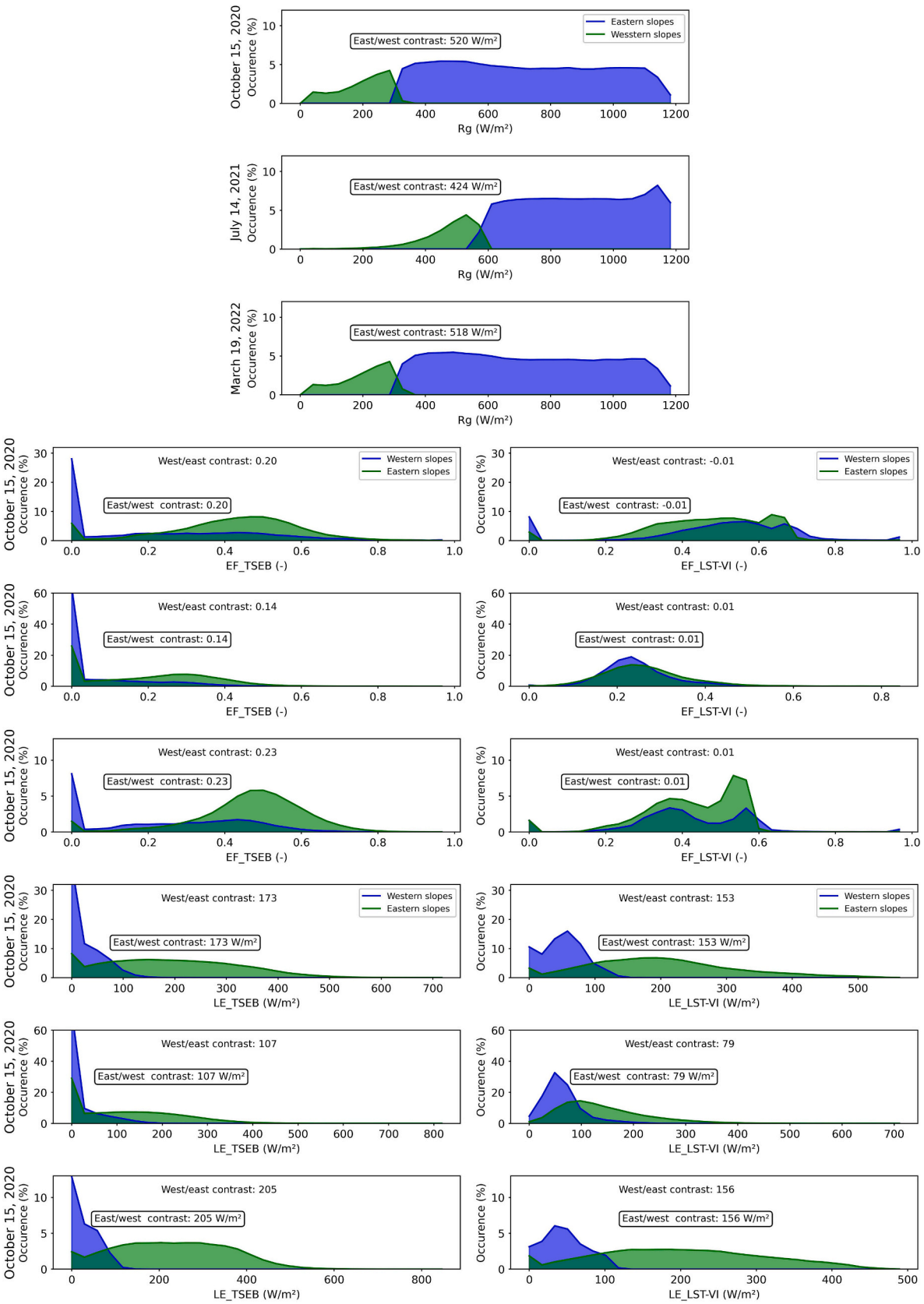

Fig. 12. Distribution of Rg (top panel), LE (central panel), and EF (bottom panel) across the dry, wet, and intermediate conditions of the three selected dates (shown in rows 1–3 for each panel). Results from the TSEB-PT model are presented in the left column, juxtaposed with those from the LST-VI model in the right column. Eastern slopes are differentiated in green, while western ones in blue. (For interpretation of the references to colour in this figure legend, the reader is referred to the web version of this article.)

Table 5
The overall relative sensitivity, S_p, of the TSEB_PT and LST-VI models to the uncertainties in the required inputs for estimating LE at the Tazaghart and Tahanaout sites.

Altered input	% change	TSEB_PT		LST_VI	
		Tahanaout site	Tazaghart site	Tahanaout site	Tazaghart site
LST	± 5 %	**0.34**	**0.66**	0.05	0.08
	± 7.5 %	**0.52**	**0.92**	0.08	0.14
	± 10 %	**0.67**	**1.18**	0.12	0.20
	± 12.5 %	**0.80**	**1.44**	0.15	**0.26**
	± 15 %	**0.91**	**1.66**	0.19	**0.33**
Ta	± 5 %	**0.28**	0.17	0.05	0.06
	± 7.5 %	**0.43**	**0.26**	0.08	0.11
	± 10 %	**0.57**	**0.35**	0.12	0.16
	± 12.5 %	**0.71**	**0.43**	0.15	**0.21**
	± 15 %	**0.83**	**0.52**	0.19	**0.26**
Rg	± 5 %	**0.21**	**0.45**	0.14	0.18
	± 10 %	**0.42**	**0.76**	**0.27**	**0.36**
	± 15 %	**0.63**	**1.14**	**0.41**	**0.54**
	± 20 %	**0.85**	**1.21**	**0.55**	**0.72**
	± 25 %	**1.04**	**1.34**	**0.68**	**0.91**
Ws	± 5 %	0.03	0.15	0.01	0.02
	± 10 %	0.07	**0.31**	0.02	0.05
	± 15 %	0.11	**0.45**	0.03	0.07
	± 20 %	0.15	**0.58**	0.04	0.10
	± 25 %	0.18	**0.69**	0.05	0.12
Rh	± 5 %	0.02	0	0	0
	± 10 %	0.04	0	0	0
	± 15 %	0.06	0.01	0.01	0.02
	± 20 %	0.07	0.01	0.02	0.05
	± 25 %	0.09	0.02	0.03	0.07

For the TSEB_PT model, errors in LST and Rg have the greatest influence on LE at both sites. At Tahanaout, S_p values reach 0.91 at ±15 % for LST and 1.04 at ±25 % for Rg, corresponding to LE changes of up to 58 % and 57 %, respectively. Ta also significantly influences LE at Tahanaout, with an S_p value of 0.83 at ±15 %, corresponding to an LE change of up to 51 %. At the elevated Tazaghart site, the sensitivity to LST and Rg becomes even more pronounced, with Sp values of 1.66 at ±15 % for LST and 1.34 at ±25 % for Rg, resulting in LE changes of up to 101 % for LST and 67 % for Rg. In contrast, the influence of Ta decreases at Tazaghart, with an S_p value of 0.52 at ±15 %.

number of high-resolution inputs each having their own uncertainties. The land-cover data required to characterize the canopy structure and surface aerodynamic properties (Raupach, 1994; Kustas et al., 1994; Kustas and Norman, 2000) is based on the static CGLS land cover map at global scale (Table 2). Despite the reduced spatial resolution between the Landsat data and the CGLS map (30 m and 100 m, respectively), and the fact that the CGLS map is reclassified and updated for each satellite pass, a closer examination revealed several inconsistencies. In particular discrepancies were found between the land cover type flagged by the map and the actual type at the elevated parts as well as the foothills in the study. For instance, the CGLS map flagged large fields as cropland, thus a maximum height of 1.2 m, but actually those fields are trees of 3 to 4 m tall regularly spaced by about 3 m. Another example, in the riparian part of the steep-sided valleys, trees with understory apparent crops on very high-resolution imagery were flagged as closed evergreen broadleaf trees and assumed not to be clumped. In addition, the prescribed values that were assigned in Table 2 are very general, as they are trying to fit a global-based land cover legend. Therefore, they can significantly deviate from the pixel's actual values. However, the LST-VI method doesn't rely on these input parameters, which makes it insensitive to the potential inaccuracies they might introduce.

While every effort is made in this study to ensure precision in spatializing meteorological forcing through various processes like modeling, disaggregation, and resampling, it inevitably introduces added uncertainty to the TSEB-PT modeled ET.

5. Summary and conclusion

Mountains, often termed 'water towers', are pivotal for hydrological studies. However, using thermal infrared data to estimate ET in such terrains remains largely unexplored. In the rugged terrain of the High Atlas mountain range in Morocco, we adapted, rigorously evaluated, and intercompared two thermal-based ET models: the EB-based TSEB-PT model and an EF-based model using the LST-VI feature space. The TSEB-PT model requires the spatialization of meteorological data and input parameters at the thermal sensor's resolution. In contrast, the LST-VI model necessitates prior normalization of LST data to account for topography-induced variability in meteorological forcings before estimating EF and ET. Using 30 m resolution LST data derived from the Landsat constellation (C2L2 resampled product) and spatialized meteorological products (Rg, Ta, Rh, and Ws), we focused our assessments on two EC sites: Tahanaout, an agricultural foothill site, and Tazaghart, located near North Africa's highest summit.

Key findings from this study can be concisely summarized as follows:

(i). Energy fluxes from both models demonstrate substantial agreement with measurements. In terms of LE, the TSEB-PT model provided an RMSE of 50 W/m^2 at the elevated site and 70 W/m^2 at the piedmont site. Concurrently, the normalized LST-VI model achieved an RMSE of 45 W/m^2 and 52 W/m^2 at the respective sites.

(ii). When accounting for topographic effects, there was a significant reduction in the uncertainty of ET retrievals at the elevated site, with a 50 % and 59 % reduction in RMSE for TSEB-PT and LST-VI model respectively. Conversely, at the piedmont site, despite its gentler topography, the uncertainties in retrieved ET were still notably reduced, showing a 29 % and 16 % reduction in RMSE for TSEB-PT and LST-VI model respectively.

(iii). Normalizing LST data for topographical effects enabled the LST-VI approach to operate effectively in mountainous terrains but also to achieve an accuracy in ET estimates that marginally surpassed that achieved by TSEB-PT.

(iv). Spatial analysis showed general agreement between the two models in the distribution of LE under varying soil moisture conditions within the study area. However, in regions with steep slopes, minor spatial discrepancies were observed. In particular, the distributions of EF simulated by LST-VI model are quite consistent on east- and west-facing slopes with an average

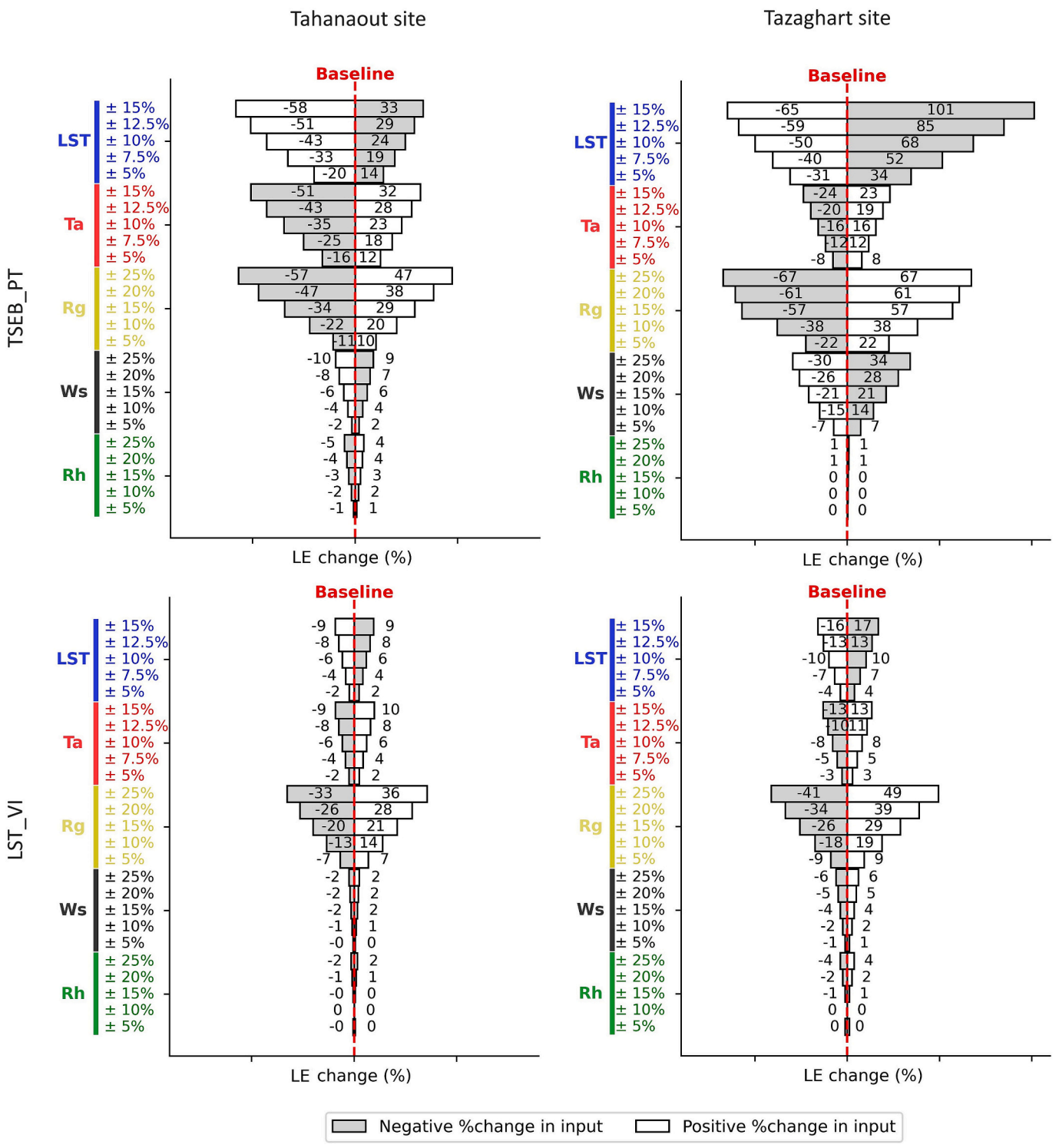

Fig. 13. Percentage change in LE estimates by the TSEB_PT model (top row) and LST_VI model (bottom row) in response to artificially perturbed inputs, assumed to reflect topography-induced variations. Results are presented for the Tahanaout site (left column) and the Tazaghart site (right column).

difference of 0.01, whereas this difference is significantly greater (an average of 0.19) for the EF simulated by TSEB_PT. This tends to indicate that the LST-VI-based approach is less sensitive to uncertainties in fine-scale meteorological data – through the normalization procedure of LST data for meteorological conditions within the study area– than the EB-based model operating at the pixel scale.

(v). Sensitivity analysis showed that the LST-VI model is less sensitive to input perturbations compared to the TSEB-PT model due to three main factors: the contextual approach requires fewer inputs than physically-based models, EF and Rn estimations are independent in the LST-VI model, and the LST normalization process has reduced sensitivity. The variability in EF between east- and west-facing slopes observed in the TSEB-PT model is mainly due to its sensitivity to variations in LST and, to a lesser extent to Ws.

Knowledge of meteorological conditions at fine scale is essential for a practical application of this methodology across extensive mountainous

terrains. Integration of advanced, computationally efficient versions of radiative transfer models, such as the evolving DART model, will overcome the limitations of empirical models and pave the way for enhanced Rg estimates in topographically complex regions. Care must be taken when using satellite-derived LST to drive EB-based models in areas with steep slopes. Further research is especially needed to improve the spatialization of Ws. This would require the development of high-resolution 3D Ws products or models that account for the mountains' unique Ws patterns (e.g., breezes, downslope winds, Foehn or Chinook winds …). Caution is also advised when using C2L2 resampled 30 m resolution TIRS data in highly heterogeneous sites, or the implementation of approaches at the native TIRS resolution should be considered to guarantee accuracy.

The limitations in the TSEB-PT model are mainly associated with the accumulated uncertainties stemming from the substantial number of variables and parameters required for its operation, and from the use of meteorological data as input at the pixel scale. For instance, refining resistance parameters could potentially improve heat flux estimation, but is proving difficult in these mountainous regions, particularly for areas with low vegetation cover on slopes. As to the LST-VI approach, it is notably based on the principle that the extreme temperatures of vegetation are representative of all vegetation types, whatever their height. However, in reality, the maximum temperature of low vegetation subjected to maximum stress may be very different from that of high vegetation subjected to similar stress conditions. Consequently, taking these factors into account could improve the identification of the dry edge and, ultimately, the estimation of EF and ET. As a significant perspective, the methodology to implement thermal-based ET models at high resolution in mountainous areas could be useful in the context of upcoming global satellite missions such as TRISHNA (CNES/ISRO, France, India) (Lagouarde et al., 2018), VanZyl-1 (Hydrosat, USA) (Lalli et al., 2022), LSTM (ESA, Europe) (Koetz et al., 2018), and SBG (NASA, USA) (Shreevastava et al., 2023). These upcoming missions will supply thermal infrared data at high spatial (down to a dozen meters and temporal (a frequency ranging from daily when combined to several times per week) resolution. Such advances could herald a new era in the use of thermal remote sensing to describe hydrological functioning in these complex landscapes.

CRediT authorship contribution statement

Badr-eddine Sebbar: Conceptualization, Data curation, Formal analysis, Investigation, Methodology, Software, Validation, Visualization, Writing – original draft, Writing – review & editing. **Yoann Malbéteau:** Conceptualization, Formal analysis, Methodology, Software, Writing – original draft, Writing – review & editing. **Saïd Khabba:** Conceptualization, Formal analysis, Funding acquisition, Investigation, Methodology, Resources, Supervision, Validation, Writing – original draft, Writing – review & editing. **Marine Bouchet:** Methodology, Software, Writing – original draft, Writing – review & editing. **Vincent Simonneaux:** Formal analysis, Investigation, Resources, Supervision, Validation, Writing – original draft, Writing – review & editing. **Abdelghani Chehbouni:** Funding acquisition, Project administration, Resources, Supervision, Writing – original draft, Writing – review & editing. **Olivier Merlin:** Conceptualization, Formal analysis, Funding acquisition, Investigation, Methodology, Project administration, Supervision, Validation, Writing – original draft, Writing – review & editing.

Declaration of competing interest

The authors declare that they have no known competing financial interests or personal relationships that could have appeared to influence the work reported in this paper.

Acknowledgement

This study was financially supported by the projects: Horizon 2020 ACCWA (grant agreement no: 823965) in the context of Marie Sklodowska-Curie research and the innovation staff exchange (RISE) program, and PRIMA-S2-ALTOS-2018 "Managing water resources within Mediterranean agrosystems by accounting for spatial structures and connectivities", and APR&D multithématique 2020 CNRST-FOCP/GEANTech "Gestion durable de l'Eau en Agriculture: Innovation d'une approche synergique des Nouvelles Technologies et d'intelligence collective". In addition, the main author gratefully acknowledges the scholarship support from Mohammed VI Polytechnic University. The authors also acknowledge the data provided by the the Tensift Observatory in the frame of the SudMed project and the TREMA International Joint Laboratory (https://www.lmi-trema.ma/ last accessed 15/10/2023) funded by the University Cadi Ayyad (UCA, Morocco) and the French Research Institute for Development (IRD, CESBIO Laboratory, France).

Data availability

The authors do not have permission to share data.

References

Allen, R.G., Pereira, L.S., Raes, D., Smith, M., 1998. Crop evapotranspiration-guidelines for computing crop water requirements-FAO irrigation and drainage paper 56. Fao, Rome 300 (9), D05109.

Allen, R.G., Tasumi, M., Trezza, R., 2007. Satellite-based energy balance for mapping evapotranspiration with internalized calibration (METRIC)—model. J. Irrig. Drain. Eng. 133 (4), 380–394. https://doi.org/10.1061/(asce)0733-9437(2007)133:4(380).

Anderson, M.C., Norman, J.M., Diak, G.R., Kustas, W.P., Mecikalski, J.R., 1997. A two-source time-integrated model for estimating surface fluxes using thermal infrared remote sensing. Remote Sens. Environ. 60 (2), 195–216. https://doi.org/10.1016/s0034-4257(96)00215-5.

Anderson, M.C., Norman, J.M., Kustas, W.P., Houborg, R., Starks, P.J., Agam, N., 2008. A thermal-based remote sensing technique for routine mapping of land-surface carbon, water and energy fluxes from field to regional scales. Remote Sens. Environ. 112 (12), 4227–4241. https://doi.org/10.1016/j.rse.2008.07.009.

Baba, M.W., Gascoin, S., Kinnard, C., Marchane, A., Hanich, L., 2019. Effect of digital elevation model resolution on the simulation of the snow cover evolution in the high atlas. Water Resour. Res. 55 (7), 5360–5378. https://doi.org/10.1029/2018wr023789.

Bartholic, J.F., Namken, L.N., Wiegand, C.L., 1972. Aerial thermal scanner to determine temperatures of soils and of crop canopies differing in water stress 1. Agron. J. 64 (5), 603–608. https://doi.org/10.2134/agronj1972.00021962006400050016x.

Bastiaanssen, W.G., Menenti, M., Feddes, R.A., Holtslag, A.A.M., 1998a. A remote sensing surface energy balance algorithm for land (SEBAL). 1. Formulation. J. Hydrol. 212, 198–212. https://doi.org/10.1016/s0022-1694(98)00253-4.

Bastiaanssen, W.G., Pelgrum, H., Wang, J., Ma, Y., Moreno, J.F., Roerink, G.J., Van der Wal, T., 1998b. A remote sensing surface energy balance algorithm for land (SEBAL).: part 2: validation. J. Hydrol. 212, 213–229. https://doi.org/10.1016/s0022-1694(98)00254-6.

Bristow, K.L., 1987. On solving the surface energy balance equation for surface temperature. Agric. For. Meteorol. 39 (1), 49–54. https://doi.org/10.1016/0168-1923(87)90015-3.

Brown, K.W., 1975. Calculations of evapotranspiration from crop surface temperature. In: Developments in Agricultural and Managed Forest Ecology, vol. 1. Elsevier, pp. 199–209. https://doi.org/10.1016/b978-0-444-41273-7.50020-9.

Buchhorn, M., Lesiv, M., Tsendbazar, N.E., Herold, M., Bertels, L., Smets, B., 2020. Copernicus global land cover layers—collection 2. Remote Sens. 12 (6), 1044. https://doi.org/10.3390/rs12061044.

Campbell, G.S., 1986. Extinction coefficients for radiation in plant canopies calculated using an ellipsoidal inclination angle distribution. Agric. For. Meteorol. 36 (4), 317–321.

Carlson, T.N., Capehart, W.J., Gillies, R.R., 1995. A new look at the simplified method for remote sensing of daily evapotranspiration. Remote Sens. Environ. 54 (2), 161–167. https://doi.org/10.1016/0034-4257(95)00139-r.

Castelli, M., Anderson, M.C., Yang, Y., Wohlfahrt, G., Bertoldi, G., Niedrist, G., Notarnicola, C., 2018. Two-source energy balance modeling of evapotranspiration in alpine grasslands. Remote Sens. Environ. 209, 327–342. https://doi.org/10.1016/j.rse.2018.02.062.

Chaponnière, A., Boulet, G., Chehbouni, A., Aresmouk, M., 2008. Understanding hydrological processes with scarce data in a mountain environment. Hydrol. Process: An International Journal 22 (12), 1908–1921. https://doi.org/10.1002/hyp.6775.

Cheggour, A., Simonneaux, V., Asma, S., Yaro, Y., Sadik, E., Sabir, M., Roose, E., 2008. Recherche d'indicateurs de ruissellement et des risques d'érosion au moyen de tests

d'infiltrométrie dans le bassin versant du Rhéraya (Haut-Atlas occidental, Maroc). Revue des Sciences de l'Eau 21 (3), 311–322. https://doi.org/10.7202/018777ar.
Chehbouni, A., Escadafal, R., Duchemin, B., Boulet, G., Simonneaux, V., Dedieu, G., et al., 2008. An integrated modelling and remote sensing approach for hydrological study in arid and semi-arid regions: the SUDMED Programme. Int. J. Remote Sens. 29 (17–18), 5161–5181. https://doi.org/10.1080/01431160802036417.
Chen, J.M., Liu, J., 2020. Evolution of evapotranspiration models using thermal and shortwave remote sensing data. Remote Sens. Environ. 237, 111594. https://doi.org/10.1016/j.rse.2019.111594.
Chen, T., & Guestrin, C. (2015, August). Xgboost: Reliable large-scale tree boosting system. In *Proceedings of the 22nd SIGKDD Conference on Knowledge Discovery and Data Mining*, San Francisco, CA, USA (pp. 13-17). https://doi.org/10.1145/2939672.2939785.
Chu, H., Luo, X., Ouyang, Z., Chan, W.S., Dengel, S., Biraud, S.C., et al., 2021. Representativeness of Eddy-covariance flux footprints for areas surrounding AmeriFlux sites. Agric. For. Meteorol. 301, 108350. https://doi.org/10.1016/j.agrformet.2021.108350.
Clothier, B.E., Clawson, K.L., Pinter Jr., P.J., Moran, M.S., Reginato, R.J., Jackson, R.D., 1986. Estimation of soil heat flux from net radiation during the growth of alfalfa. Agric. For. Meteorol. 37 (4), 319–329. https://doi.org/10.1016/0168-1923(86)90069-9.
de Tomás, A., Nieto, H., Guzinski, R., Salas, J., Sandholt, I., Berliner, P., 2014. Validation and scale dependencies of the triangle method for the evaporative fraction estimation over heterogeneous areas. Remote Sens. Environ. 152, 493–511. https://doi.org/10.1016/j.rse.2014.06.028.
Evin, G., Le Lay, M., Fouchier, C., Penot, D., Colleoni, F., Mas, A., et al., 2024. Evaluation of hydrological models on small mountainous catchments: impact of the meteorological forcings. Hydrol. Earth Syst. Sci. 28 (1), 261–281. https://doi.org/10.5194/hess-28-261-2024.
Firozjaei, M.K., Fathololoumi, S., Alavipanah, S.K., Kiavarz, M., Vaezi, A.R., Biswas, A., 2020. A new approach for modeling near surface temperature lapse rate based on normalized land surface temperature data. Remote Sens. Environ. 242, 111746. https://doi.org/10.1016/j.rse.2020.111746.
Fisher, J.B., Tu, K.P., Baldocchi, D.D., 2008. Global estimates of the land–atmosphere water flux based on monthly AVHRR and ISLSCP-II data, validated at 16 FLUXNET sites. Remote Sens. Environ. 112 (3), 901–919. https://doi.org/10.1016/j.rse.2007.06.025.
Floors, R., Badger, M., Troen, I., Grogan, K., Permien, F.H., 2021. Satellite-based estimation of roughness lengths and displacement heights for wind resource modelling. Wind Energy Sci. 6 (6), 1379–1400. https://doi.org/10.5194/wes-6-1379-2021.
Foken, T., Aubinet, M., Finnigan, J.J., Leclerc, M.Y., Mauder, M., Paw, U., K. T, 2011. Results of a panel discussion about the energy balance closure correction for trace gases. Bull. Am. Meteorol. Soc. 92 (4), ES13–ES18. https://doi.org/10.1175/2011bams3130.1.
Franks, S., Storey, J., Rengarajan, R., 2020. The new landsat collection-2 digital elevation model. Remote Sens. 12 (23), 3909. https://doi.org/10.3390/rs12233909.
Gao, Z.Q., Liu, C.S., Gao, W., Chang, N.B., 2011. A coupled remote sensing and the surface energy balance with topography algorithm (SEBTA) to estimate actual evapotranspiration over heterogeneous terrain. Hydrol. Earth Syst. Sci. 15 (1), 119–139. https://doi.org/10.5194/hess-15-119-2011.
Gastellu-Etchegorry, J.P., Martin, E., Gascon, F., 2004. DART: a 3D model for simulating satellite images and studying surface radiation budget. Int. J. Remote Sens. 25 (1), 73–96. https://doi.org/10.1080/0143116031000115166.
Gillies, R.R., Kustas, W.P., Humes, K.S., 1997. A verification of the 'triangle' method for obtaining surface soil water content and energy fluxes from remote measurements of the normalized difference vegetation index (NDVI) and surface e. Int. J. Remote Sens. 18 (15), 3145–3166. https://doi.org/10.1080/014311697217026.
Gokmen, M., Vekerdy, Z., Verhoef, A., Verhoef, W., Batelaan, O., van der Tol, C., 2012. Integration of soil moisture in SEBS for improving evapotranspiration estimation under water stress conditions. Remote Sens. Environ. 121, 261–274. https://doi.org/10.1016/j.rse.2012.02.003.
Goward, S.N., Cruickshanks, G.D., Hope, A.S., 1985. Observed relation between thermal emission and reflected spectral radiance of a complex vegetated landscape. Remote Sens. Environ. 18 (2), 137–146. https://doi.org/10.1016/0034-4257(85)90044-6.
Gutman, G., Ignatov, A., 1998. The derivation of the green vegetation fraction from NOAA/AVHRR data for use in numerical weather prediction models. Int. J. Remote Sens. 19 (8), 1533–1543. https://doi.org/10.1080/014311698215333.
Guzinski, R., Nieto, H., 2019. Evaluating the feasibility of using Sentinel-2 and Sentinel-3 satellites for high-resolution evapotranspiration estimations. Remote Sens. Environ. 221, 157–172. https://doi.org/10.1016/j.rse.2018.11.019.
Guzinski, R., Anderson, M.C., Kustas, W.P., Nieto, H., Sandholt, I., 2013. Using a thermal-based two source energy balance model with time-differencing to estimate surface energy fluxes with day–night MODIS observations. Hydrol. Earth Syst. Sci. 17 (7), 2809–2825. https://doi.org/10.5194/hess-17-2809-2013.
Guzinski, R., Nieto, H., Sandholt, I., Karamitilios, G., 2020. Modelling high-resolution actual evapotranspiration through Sentinel-2 and Sentinel-3 data fusion. Remote Sens. 12 (9), 1433. https://doi.org/10.3390/rs12091433.
Guzinski, R., Nieto, H., Sánchez, J.M., López-Urrea, R., Boujnah, D.M., Boulet, G., 2021. Utility of copernicus-based inputs for actual evapotranspiration modeling in support of sustainable water use in agriculture. IEEE J Sel. Top. Appl. Earth Obs. Remote Sens. 14, 11466–11484. https://doi.org/10.1109/jstars.2021.3122573.
Hais, M., Kučera, T., 2009. The influence of topography on the forest surface temperature retrieved from Landsat TM, ETM+ and ASTER thermal channels. ISPRS J. Photogramm. Remote Sens. 64 (6), 585–591. https://doi.org/10.1016/j.isprsjprs.2009.04.003.
Han, C., Ma, Y., Wang, B., Zhong, L., Ma, W., Chen, X., Su, Z., 2021. Long-term variations in actual evapotranspiration over the Tibetan plateau. Earth Syst. Sci. Data. 13 (7), 3513–3524. https://doi.org/10.5194/essd-13-3513-2021.
Hanich, L., Chehbouni, A., Gascoin, S., Boudhar, A., Jarlan, L., Tramblay, Y., Khabba, S., 2022. Snow hydrology in the Moroccan Atlas Mountains. J. Hydrol. Reg. Stud. 42, 101101. https://doi.org/10.1016/j.ejrh.2022.101101.
Hao, D., Bisht, G., Gu, Y., Lee, W.L., Liou, K.N., Leung, L.R., 2021. A parameterization of sub-grid topographical effects on solar radiation in the E3SM land model (version 1.0): implementation and evaluation over the Tibetan plateau. Geosci. Model Dev. 14 (10), 6273–6289. https://doi.org/10.5194/gmd-14-6273-2021.
Heilman, J.L., Kanemasu, E.T., Rosenberg, N.J., Blad, B.L., 1976. Thermal scanner measurement of canopy temperatures to estimate evapotranspiration. Remote Sens. Environ. 5, 137–145. https://doi.org/10.1016/0034-4257(76)90044-4.
Immerzeel, W.W., Van Beek, L.P., Bierkens, M.F., 2010. Climate change will affect the Asian water towers. Science 328 (5984), 1382–1385. https://doi.org/10.1126/science.1183188.
Ingenhorst, C., Jacobs, G., Stößel, L., Schelenz, R., Juretzki, B., 2021. Method for airborne measurement of the spatial wind speed distribution above complex terrain. Wind Energy Sci. 6 (2), 427–440. https://doi.org/10.5194/wes-2020-25.
Jarlan, L., Khabba, S., Er-Raki, S., Le Page, M., Hanich, L., Fakir, Y., et al., 2015. Remote sensing of water resources in semi-arid Mediterranean areas: the joint international laboratory TREMA. Int. J. Remote Sens. 36 (19–20), 4879–4917. https://doi.org/10.1080/01431161.2015.1093198.
Jiang, L., Islam, S., 1999. A methodology for estimation of surface evapotranspiration over large areas using remote sensing observations. Geophys. Res. Lett. 26, 2773–2776. https://doi.org/10.1029/1999gl006049.
Jiang, L., Islam, S., 2001. Estimation of surface evaporation map over southern Great Plains using remote sensing data. Water Resour. Res. 37 (2), 329–340. https://doi.org/10.1029/2000wr900255.
Jung, M., Reichstein, M., Ciais, P., Seneviratne, S.I., Sheffield, J., Goulden, M.L., et al., 2010. Recent decline in the global land evapotranspiration trend due to limited moisture supply. Nat 467 (7318), 951–954. https://doi.org/10.1038/nature09396.
Kljun, N., Calanca, P., Rotach, M.W., Schmid, H.P., 2015. A simple two-dimensional parameterisation for flux footprint prediction (FFP). Geosci. Model Dev. 8 (11), 3695–3713. https://doi.org/10.5194/gmd-8-3695-2015.
Koetz, B., Bastiaanssen, W., Berger, M., Defourney, P., Del Bello, U., Drusch, M., Udelhoven, T., 2018, July. High spatio-temporal resolution land surface temperature mission-a copernicus candidate mission in support of agricultural monitoring. In: Igarss 2018–2018 IEEE Int. Geosci. Remote Sens. Symp. IEEE, pp. 8160–8162. https://doi.org/10.1109/igarss.2018.8517433.
Kool, D., Agam, N., Lazarovitch, N., Heitman, J.L., Sauer, T.J., Ben-Gal, A., 2014. A review of approaches for evapotranspiration partitioning. Agric. For. Meteorol. 184, 56–70. https://doi.org/10.1016/j.agrformet.2013.09.003.
Kustas, W., Anderson, M., 2009. Advances in thermal infrared remote sensing for land surface modeling. Agric. For. Meteorol. 149 (12), 2071–2081. https://doi.org/10.1016/j.agrformet.2009.05.016.
Kustas, W.P., Daughtry, C.S., 1990. Estimation of the soil heat flux/net radiation ratio from spectral data. Agric. For. Meteorol. 49 (3), 205–223. https://doi.org/10.1016/0168-1923(90)90033-3.
Kustas, W.P., Norman, J.M., 1999. Evaluation of soil and vegetation heat flux predictions using a simple two-source model with radiometric temperatures for partial canopy cover. Agric. For. Meteorol. 94 (1), 13–29. https://doi.org/10.1016/s0168-1923(99)00005-2.
Kustas, W.P., Norman, J.M., 2000. A two-source energy balance approach using directional radiometric temperature observations for sparse canopy covered surfaces. Agron. J. 92 (5), 847–854. https://doi.org/10.2134/agronj2000.925847x.
Kustas, W.P., Choudhury, B.J., Moran, M.S., Reginato, R.J., Jackson, R.D., Gay, L.W., Weaver, H.L., 1989. Determination of sensible heat flux over sparse canopy using thermal infrared data. Agric. For. Meteorol. 44 (3–4), 197–216. https://doi.org/10.1016/0168-1923(89)90017-8.
Kustas, W.P., Blanford, J.H., Stannard, D.I., Daughtry, C.S., Nichols, W.D., Weltz, M.A., 1994. Local energy flux estimates for unstable conditions using variance data in semiarid rangelands. Water Resour. Res. 30 (5), 1351–1361. https://doi.org/10.1029/93wr03084.
Lagouarde, J.P., Bhattacharya, B.K., Crebassol, P., Gamet, P., Babu, S.S., Boulet, G., et al., 2018, July. The Indian-French Trishna mission: Earth observation in the thermal infrared with high spatio-temporal resolution. In: IGARSS 2018–2018 IEEE Int. Geosci. Remote Sens. Symp. IEEE, pp. 4078–4081. https://doi.org/10.1109/igarss.2018.8518720.
Lalli, K., Soenen, S., Fisher, J., McGlinchy, J., Kleynhans, T., Eon, R., Moreau, L.M., 2022, September. VanZyl-1: Demonstrating SmallSat measurement capabilities for land surface temperature and evapotranspiration. In: CubeSats and SmallSats for Remote Sensing *vI*, 12236. SPIE, pp. 25–36. https://doi.org/10.1117/12.2632565.
Liston, G.E., Elder, K., 2006. A meteorological distribution system for high-resolution terrestrial modeling (MicroMet). J. Hydrometeorol. 7, 217–234. https://doi.org/10.1175/jhm486.1.
Long, D., Singh, V.P., 2012. A two-source trapezoid model for evapotranspiration (TTME) from satellite imagery. Remote Sens. Environ. 121, 370–388. https://doi.org/10.1016/j.rse.2012.02.015.
Long, D., Singh, V.P., Scanlon, B.R., 2012. Deriving theoretical boundaries to address scale dependencies of triangle models for evapotranspiration estimation. J. Geophys. Res. Atmos. 117 (D5). https://doi.org/10.1029/2011jd017079.
Magnus, G., 1844. Versuche über die Spannkräfte des Wasserdampfes. Ann. Phys. Chem. 61 (5), 225–247. https://doi.org/10.1002/andp.18441370202.
Majozi, N.P., Mannaerts, C.M., Ramoelo, A., Mathieu, R., Mudau, A.E., Verhoef, W., 2017. An intercomparison of satellite-based daily evapotranspiration estimates

under different eco-climatic regions in South Africa. Remote Sens. 9 (4), 307. https://doi.org/10.3390/rs9040307.
Malbéteau, Y., Merlin, O., Gascoin, S., Gastellu, J.P., Mattar, C., Olivera-Guerra, L., et al., 2017. Normalizing land surface temperature data for elevation and illumination effects in mountainous areas: a case study using ASTER data over a steep-sided valley in Morocco. Remote Sens. Environ. 189, 25–39. https://doi.org/10.1016/j.rse.2016.11.010.
Marchane, A., Jarlan, L., Hanich, L., Boudhar, A., Gascoin, S., Tavernier, A., et al., 2015. Assessment of daily MODIS snow cover products to monitor snow cover dynamics over the Moroccan atlas mountain range. Remote Sens. Environ. 160, 72–86. https://doi.org/10.1016/j.rse.2015.01.002.
Mbabazi, D., Mohanty, B.P., Gaur, N., 2023. High spatio-temporal resolution evapotranspiration estimates within large agricultural fields by fusing eddy covariance and Landsat based data. Agric. For. Meteorol. 333, 109417. https://doi.org/10.1016/j.agrformet.2023.109417.
Merlin, O., 2013. An original interpretation of the wet edge of the surface temperature–albedo space to estimate crop evapotranspiration (SEB-1S), and its validation over an irrigated area in northwestern Mexico. Hydrol. Earth Syst. Sci. 17 (9), 3623–3637. https://doi.org/10.5194/hess-17-3623-2013.
Merlin, O., Chehbouni, A., 2004. Different approaches in estimating heat flux using dual angle observations of radiative surface temperature. Int. J. Remote Sens. 25 (1), 275–289. https://doi.org/10.1080/0143116031000116408.
Merlin, O., Walker, J.P., Chehbouni, A., Kerr, Y., 2008. Towards deterministic downscaling of SMOS soil moisture using MODIS derived soil evaporative efficiency. Remote Sens. Environ. 112 (10), 3935–3946. https://doi.org/10.1016/j.rse.2008.06.012.
Merlin, O., Chirouze, J., Olioso, A., Jarlan, L., Chehbouni, G., Boulet, G., 2014. An image-based four-source surface energy balance model to estimate crop evapotranspiration from solar reflectance/thermal emission data (SEB-4S). Agric. For. Meteorol. 184, 188–203. https://doi.org/10.1016/j.agrformet.2013.10.002.
Minacapilli, M., Consoli, S., Vanella, D., Ciraolo, G., Motisi, A., 2016. A time domain triangle method approach to estimate actual evapotranspiration: application in a Mediterranean region using MODIS and MSG-SEVIRI products. Remote Sens. Environ. 174, 10–23. https://doi.org/10.1016/j.rse.2015.12.018.
Miralles, D.G., Holmes, T.R.H., De Jeu, R.A.M., Gash, J.H., Meesters, A.G.C.A., Dolman, A.J., 2011. Global land-surface evaporation estimated from satellite-based observations. Hydrol. Earth Syst. Sci. 15 (2), 453–469. https://doi.org/10.5194/hess-15-453-2011.
Monteith, J., Unsworth, M., 2013. Principles of environmental physics: plants, animals, and the atmosphere. Academic Press. https://doi.org/10.1016/b978-0-12-386910-4.00017-2.
Morillas, L., García, M., Nieto, H., Villagarcia, L., Sandholt, I., Gonzalez-Dugo, M.P., et al., 2013. Using radiometric surface temperature for surface energy flux estimation in Mediterranean drylands from a two-source perspective. Remote Sens. Environ. 136, 234–246. https://doi.org/10.1016/j.rse.2013.05.010.
Mu, Q., Zhao, M., Running, S.W., 2011. Improvements to a MODIS global terrestrial evapotranspiration algorithm. Remote Sens. Environ. 115 (8), 1781–1800. https://doi.org/10.1016/j.rse.2011.02.019.
Muñoz-Sabater, J., Dutra, E., Agustí-Panareda, A., Albergel, C., Arduini, G., Balsamo, G., et al., 2021. ERA5-land: a state-of-the-art global reanalysis dataset for land applications. Earth Syst. Sci. Data. 13 (9), 4349–4383. https://doi.org/10.5194/essd-13-4349-2021.
Nemani, R.R., Running, S.W., 1989. Estimation of regional surface resistance to evapotranspiration from NDVI and thermal-IR AVHRR data. J. Appl. Meteorol. 28, 276–284. https://doi.org/10.1175/1520-0450(1989)028<0276:eorsrt>2.0.co;2.
Nippgen, F., McGlynn, B.L., Emanuel, R.E., Klaus, J., 2011. Landscape structure and climate influences on hydrologic response. Water Resour. Res. 47 (12). https://doi.org/10.1029/2011wr011161.
Nishida, K., Nemani, R.R., Running, S.W., Glassy, J.M., 2003. An operational remote sensing algorithm of land surface evaporation. J. Geophys. Res.-Atmos. 108 (D9), 4270. https://doi.org/10.1029/2002jd002062.
Norman, J.M., Kustas, W.P., Humes, K.S., 1995. Source approach for estimating soil and vegetation energy fluxes in observations of directional radiometric surface temperature. Agric. For. Meteorol. 77 (3–4), 263–293. https://doi.org/10.1016/0168-1923(96)02344-1.
Norman, J.M., Anderson, M.C., Kustas, W.P., French, A.N., Mecikalski, J.O.H.N., Torn, R., et al., 2003. Remote sensing of surface energy fluxes at 101-m pixel resolutions. Water Resour. Res. 39 (8). https://doi.org/10.1029/2002wr001775.
Ouassanouan, Y., Fakir, Y., Simonneaux, V., Kharrou, M.H., Bouimouass, H., Najar, I., et al., 2022. Multi-decadal analysis of water resources and agricultural change in a Mediterranean semiarid irrigated piedmont under water scarcity and human interaction. Sci. Total Environ. 834, 155328. https://doi.org/10.1016/j.scitotenv.2022.155328.
Pepin, N., Bradley, R.S., Diaz, H.F., Baraer, M., Caceres, E.B., Forsythe, N., et al., 2015. Elevation-dependent warming in mountain regions of the world. Nat. Clim. Chang. 5 (5), 424–430. https://doi.org/10.1038/nclimate2563.
PRiCE, J.C., 1990. Using spatial context in satellite data to infer regional scale evapotranspiration. IEEE Trans. Geosci. Remote Sens. 28 (5), 940–948. https://doi.org/10.1109/36.58983.
Priestley, C.H.B., Taylor, R.J., 1972. On the assessment of surface heat flux and evaporation using large-scale parameters. Mon. Weather Rev. 100 (2), 81–92. https://doi.org/10.1175/1520-0493(1972)100<0081:otaosh>2.3.co;2.
Raupach, M.R., 1994. Simplified expressions for vegetation roughness length and zero-plane displacement as functions of canopy height and area index. Bound.-Layer Meteorol. 71 (1–2), 211–216. https://doi.org/10.1007/bf00709229.
Rhoujjati, N., Brahim, Y.A., Hanich, L., Rhoujjati, A., Rafik, A., Ouatiki, H., et al., 2023. Snowpack and groundwater recharge in the atlas mountains: new evidence and key drivers. J. Hydrol. Reg. Stud. 49, 101520. https://doi.org/10.1016/j.ejrh.2023.101520.
Ryu, Y., Baldocchi, D.D., Kobayashi, H., Van Ingen, C., Li, J., Black, T.A., et al., 2011. Integration of MODIS land and atmosphere products with a coupled-process model to estimate gross primary productivity and evapotranspiration from 1 km to global scales. Glob. Biogeochem. Cycles 25 (4). https://doi.org/10.1029/2011gb004053.
Samani, Z., Bawazir, A.S., Bleiweiss, M., Skaggs, R., Tran, V.D., 2007. Estimating daily net radiation over vegetation canopy through remote sensing and climatic data. J. Irrig. Drain. Eng. 133 (4), 291–297. https://doi.org/10.1061/(asce)0733-9437(2007)133:4(291).
Sánchez, J.M., Kustas, W.P., Caselles, V., Anderson, M.C., 2008. Modelling surface energy fluxes over maize using a two-source patch model and radiometric soil and canopy temperature observations. Remote Sens. Environ. 112 (3), 1130–1143. https://doi.org/10.1016/j.rse.2007.07.018.
Sandholt, I., Andersen, H.S., 1993. Derivation of actual evapotranspiration in the Senegalese Sahel, using NOAA-AVHRR data during the 1987 growing season. Remote Sens. Environ. 46 (2), 164–172. https://doi.org/10.1016/0034-4257(93)90092-c.
Sandholt, I., Rasmussen, K., & Andersen, J. (2002). A simple interpretation of the surface temperature/vegetation index space for assessment of surface moisture status. Remote Sens. Environ., 79(2–3), 213–224. doi:https://doi.org/10.1016/s0034-4257(01)00274-7.
Schaudt, K.J., Dickinson, R.E., 2000. An approach to deriving roughness length and zero-plane displacement height from satellite data, prototyped with BOREAS data. Agric. For. Meteorol. 104 (2), 143–155. https://doi.org/10.1016/s0168-1923(00)00153-2.
Schulz, O., de Jong, C., 2004. Snowmelt and sublimation: field experiments and modelling in the high Atlas Mountains of Morocco. Hydrol. Earth Syst. Sci. 8 (6), 1076–1089. https://doi.org/10.5194/hess-8-1076-2004.
Sebbar, B.E., Khabba, S., Merlin, O., Simonneaux, V., Hachimi, C.E., Kharrou, M.H., Chehbouni, A., 2023. Machine-learning-based downscaling of hourly ERA5-land air temperature over mountainous regions. Atmosphere 14 (4), 610. https://doi.org/10.3390/atmos14040610.
Shreevastava, A., Hulley, G., Thompson, J., 2023. Algorithms for detecting sub-pixel elevated temperature features for the NASA surface biology and geology (SBG) designated observable. J. Geophys. Res. Biogeosci. 128 (7). https://doi.org/10.1029/2022jg007370 e2022JG007370.
Simonneaux, V., Cheggour, A., Deschamps, C., Mouillot, F., Cerdan, O., Le Bissonnais, Y., 2015. Land use and climate change effects on soil erosion in a semi-arid mountainous watershed (high atlas, Morocco). J. Arid Environ. 122, 64–75. https://doi.org/10.1016/j.jaridenv.2015.06.002.
Soer, G.J.R., 1980. Estimation of regional evapotranspiration and soil moisture conditions using remotely sensed crop surface temperatures. Remote Sens. Environ. 9 (1), 27–45. https://doi.org/10.1016/0034-4257(80)90045-0.
Stefan, V.G., Merlin, O., Er-Raki, S., Escorihuela, M.J., Khabba, S., 2015. Consistency between in situ, model-derived and high-resolution-image-based soil temperature endmembers: towards a robust data-based model for multi-resolution monitoring of crop evapotranspiration. Remote Sens. 7 (8), 10444–10479. https://doi.org/10.3390/rs70810444.
Stisen, S., Sandholt, I., Nørgaard, A., Fensholt, R., Jensen, K.H., 2008. Combining the triangle method with thermal inertia to estimate regional evapotranspiration—applied to MSG-SEVIRI data in the Senegal River basin. Remote Sens. Environ. 112 (3), 1242–1255. https://doi.org/10.1016/j.rse.2007.08.013.
Stone, L.R., Horton, M.L., 1974. Estimating evapotranspiration using canopy temperatures: field evaluation. Agron. J. 66 (3), 450–454. https://doi.org/10.2134/agronj1974.00021962006600030033x.
Su, Z., 2002. The surface energy balance system (SEBS) for estimation of turbulent heat fluxes. Hydrol. Earth Syst. Sci. 6 (1), 85–100. https://doi.org/10.5194/hess-6-85-2002.
Tague, C., Heyn, I., Christensen, L., 2009. Topographic controls on spatial patterns of conifer transpiration and net primary productivity under climate warming in mountain ecosystems. Ecohydrol 2 (4), 541–554. https://doi.org/10.1002/eco.88.
Tang, R., Li, Z.L., Tang, B., 2010. An application of the Ts–VI triangle method with enhanced edges determination for evapotranspiration estimation from MODIS data in arid and semi-arid regions: implementation and validation. Remote Sens. Environ. 114 (3), 540–551. https://doi.org/10.1016/j.rse.2009.10.012.
Terzago, S., Andreoli, V., Arduini, G., Balsamo, G., Campo, L., Cassardo, C., et al., 2020. Sensitivity of snow models to the accuracy of meteorological forcings in mountain environments. Hydrol. Earth Syst. Sci. 24 (8), 4061–4090. https://doi.org/10.5194/hess-24-4061-2020.
Trebs, I., Mallick, K., Bhattarai, N., Sulis, M., Cleverly, J., Woodgate, W., et al., 2021. The role of aerodynamic resistance in thermal remote sensing-based evapotranspiration models. Remote Sens. Environ. 264, 112602. https://doi.org/10.1016/j.rse.2021.112602.
Troufleau, D., Lhomme, J.P., Monteny, B., Vidal, A., 1997. Sensible heat flux and radiometric surface temperature over sparse Sahelian vegetation. I. An experimental analysis of the kB− 1 parameter. J. Hydrol. 188, 815–838. https://doi.org/10.1016/s0022-1694(96)03172-1.
Verhoef, A., De Bruin, H.A.R., Van Den Hurk, B.J.J.M., 1997. Some practical notes on the parameter kB− 1 for sparse vegetation. J. Appl. Meteorol. 36 (5), 560–572. https://doi.org/10.1175/1520-0450(1997)036<0560:spnotp>2.0.co;2.
Viviroli, D., Dürr, H.H., Messerli, B., Meybeck, M., Weingartner, R., 2007. Mountains of the world, water towers for humanity: typology, mapping, and global significance. Water Resour. Res. 43 (7). https://doi.org/10.1029/2006wr005653.

Viviroli, D., Kummu, M., Meybeck, M., Kallio, M., Wada, Y., 2020. Increasing dependence of lowland populations on mountain water resources. Nat. Sustain. 3 (11), 917–928. https://doi.org/10.1038/s41893-020-0559-9.

Volk, J.M., Huntington, J., Melton, F.S., Allen, R., Anderson, M.C., Fisher, J.B., et al., 2023. Development of a benchmark Eddy flux evapotranspiration dataset for evaluation of satellite-driven evapotranspiration models over the CONUS. Agric. For. Meteorol. 331, 109307. https://doi.org/10.1016/j.agrformet.2023.109307.

Wang, L., Parodi, G. N., & Su, Z. (2008, September). SEBS module beam: a practical tool for surface energy balance estimates from remote sensing data. In *the 2nd MERIS-(a) ATSR workshop*.

Wei, Z., Yoshimura, K., Wang, L., Miralles, D.G., Jasechko, S., Lee, X., 2017. Revisiting the contribution of transpiration to global terrestrial evapotranspiration. Geophys. Res. Lett. 44 (6), 2792–2801. https://doi.org/10.1002/2016gl072235.

Yang, K., Koike, T., Ishikawa, H., Kim, J., Li, X., Liu, H., et al., 2008. Turbulent flux transfer over bare-soil surfaces: characteristics and parameterization. J. Appl. Meteorol. Climatol. 47 (1), 276–290. https://doi.org/10.1175/2007jamc1547.1.

Yang, Y., Su, H., Zhang, R., Tian, J., Li, L., 2015. An enhanced two-source evapotranspiration model for land (ETEML): algorithm and evaluation. Remote Sens. Environ. 168, 54–65. https://doi.org/10.1016/j.rse.2015.06.020.

Zhan, X., Kustas, W.P., Humes, K.S., 1996. An intercomparison study on models of sensible heat flux over partial canopy surfaces with remotely sensed surface temperature. Remote Sens. Environ. 58 (3), 242–256. https://doi.org/10.1016/s0034-4257(96)00049-1.

Zhang, K., Kimball, J.S., Running, S.W., 2016. A review of remote sensing based actual evapotranspiration estimation. Wiley Interdiscip. Rev. Water 3 (6), 834–853. https://doi.org/10.1002/wat2.1168.

Zhao, X., Liu, Y., 2014. Relative contribution of the topographic influence on the triangle approach for evapotranspiration estimation over mountainous areas. Adv. Meteorol. 2014 (1), 584040. https://doi.org/10.1155/2014/584040.

Zhu, W., Wang, Y., Jia, S., 2023. A remote sensing-based method for daily evapotranspiration mapping and partitioning in a poorly gauged basin with arid ecosystems in the Qinghai-Tibet Plateau. J. Hydrol. 616, 128807. https://doi.org/10.1016/j.jhydrol.2022.128807.